Cell Reports

16p11.2 haploinsufficiency reduces mitochondrial biogenesis in brain endothelial cells and alters brain metabolism in adult mice

Graphical abstract

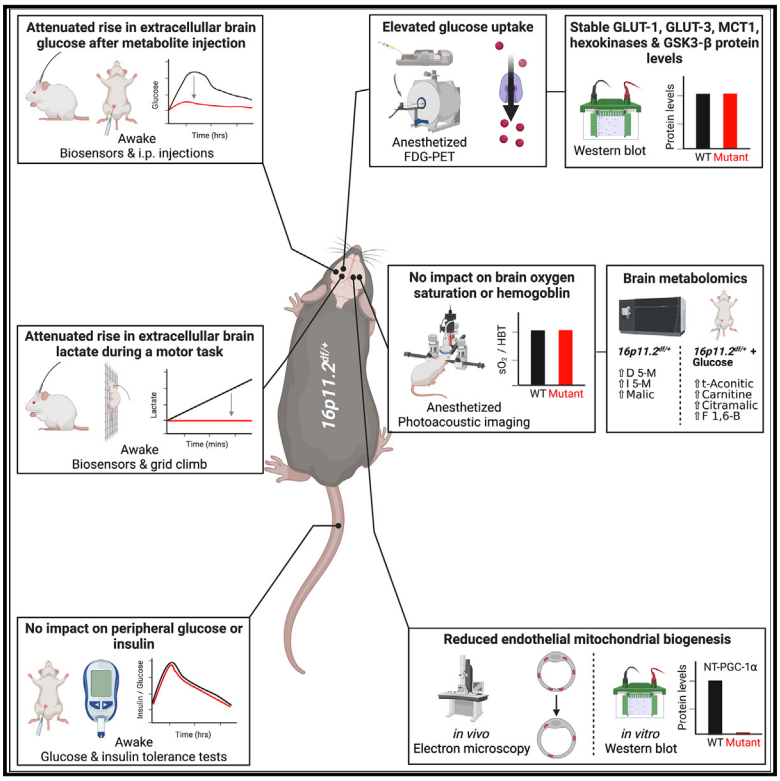

Highlights

- Constitutive 16p11.2 haploinsufficiency leads to increased brain glucose uptake
- Changes in brain metabolite flux suggest altered glycolysis or intracellular shuttling
- Brain endothelial cells from 16p11.2-deficient mice lack the NT-PGC-1α protein
- Endothelial-specific 16p11.2 haploinsufficiency leads to increased brain glucose uptake

Authors

Alexandria Béland-Millar, Alexia Kirby, Yen Truong, ..., Claude Messier, Adam J. Shuhendler, Baptiste Lacoste

Correspondence

blacoste@uottawa.ca

In brief

A mouse model of 16p11.2 deletion syndrome displays altered brain metabolism. Béland-Millar et al. show dysregulation of metabolite flux in the cerebral cortex, without concomitant differences in oxygen saturation or glucose transporters. Reduced mitochondrial biogenesis in 16p11.2-deficient brain endothelial cells appears associated with these brain metabolic changes.

Béland-Millar et al., 2023, Cell Reports *42*, 112485
May 30, 2023
https://doi.org/10.1016/j.celrep.2023.112485

CellPress

Cell Reports

CellPress
OPEN ACCESS

Report

16p11.2 haploinsufficiency reduces mitochondrial biogenesis in brain endothelial cells and alters brain metabolism in adult mice

Alexandria Béland-Millar,[1,2] Alexia Kirby,[3] Yen Truong,[4] Julie Ouellette,[1,5] Sozerko Yandiev,[6] Khalil Bouyakdan,[7] Chantal Pileggi,[8] Shama Naz,[9] Melissa Yin,[10] Micaël Carrier,[11] Pavel Kotchetkov,[1,5] Marie-Kim St-Pierre,[11] Marie-Ève Tremblay,[11,12,13] Julien Courchet,[6] Mary-Ellen Harper,[8] Thierry Alquier,[7] Claude Messier,[2] Adam J. Shuhendler,[4,14] and Baptiste Lacoste[1,5,14,15,*]

[1]Neuroscience Program, Ottawa Hospital Research Institute, Ottawa, ON, Canada
[2]School of Psychology, University of Ottawa, Ottawa, ON, Canada
[3]Faculty of Science, Department of Biology, University of Ottawa, Ottawa, ON, Canada
[4]Faculty of Science, Department of Chemistry and Biomolecular Sciences, University of Ottawa, Ottawa, ON, Canada
[5]Faculty of Medicine, Department of Cellular and Molecular Medicine, University of Ottawa, Ottawa, ON, Canada
[6]University Lyon 1, CNRS, INSERM, Physiopathologie et Génétique du Neurone et du Muscle, UMR5261, U1315, Institut NeuroMyoGène, 69008 Lyon, France
[7]Centre de Recherche du Centre Hospitalier de l'Université de Montréal (CRCHUM), Department of Medicine Université de Montréal, Montreal, QC, Canada
[8]Faculty of Medicine, Department of Biochemistry Microbiology and Immunology, Ottawa, ON, Canada
[9]University of Ottawa Metabolomics Core Facility, Faculty of Medicine, Ottawa, ON, Canada
[10]FUJIFILM VisualSonics, Inc, Toronto, ON, Canada
[11]Division of Medical Sciences, University of Victoria, Victoria, BC, Canada
[12]Neurology and Neurosurgery Department, McGill University, Montreal, QC, Canada
[13]Department of Biochemistry and Molecular Biology, The University of British Columbia, Vancouver, BC, Canada
[14]University of Ottawa Brain and Mind Research Institute, Ottawa, ON, Canada
[15]Lead contact
*Correspondence: blacoste@uottawa.ca
https://doi.org/10.1016/j.celrep.2023.112485

SUMMARY

Neurovascular abnormalities in mouse models of 16p11.2 deletion autism syndrome are reminiscent of alterations reported in murine models of glucose transporter deficiency, including reduced brain angiogenesis and behavioral alterations. Yet, whether cerebrovascular alterations in *16p11.2*$^{df/+}$ mice affect brain metabolism is unknown. Here, we report that anesthetized *16p11.2*$^{df/+}$ mice display elevated brain glucose uptake, a phenomenon recapitulated in mice with endothelial-specific 16p11.2 haplodeficiency. Awake *16p11.2*$^{df/+}$ mice display attenuated relative fluctuations of extracellular brain glucose following systemic glucose administration. Targeted metabolomics on cerebral cortex extracts reveals enhanced metabolic responses to systemic glucose in *16p11.2*$^{df/+}$ mice that also display reduced mitochondria number in brain endothelial cells. This is not associated with changes in mitochondria fusion or fission proteins, but *16p11.2*$^{df/+}$ brain endothelial cells lack the splice variant NT-PGC-1α, suggesting defective mitochondrial biogenesis. We propose that altered brain metabolism in *16p11.2*$^{df/+}$ mice is compensatory to endothelial dysfunction, shedding light on previously unknown adaptative responses.

INTRODUCTION

The brain is highly vulnerable to defects in energy intake, production, and utilization, highlighting the importance of the interplay between vascular, glial, and neuronal systems for proper function.[1–3] We recently revealed a causal relationship between endothelial deficits and neuronal abnormalities in a mouse model of the 16p11.2 deletion syndrome (*16p11.2*$^{df/+}$ mice),[4] a common mutation linked to autism spectrum disorders (ASDs).[5]

Copy number variations associated with psychiatric conditions are frequently found in the human 16p11.2 locus.[6–8] Among genes found at the 16p11.2 locus (7qF3 in mice), *AldoA* regulates glycolysis and gluconeogenesis, while *Mapk3* and *Maz1* control vascular health.[9–11] Interestingly, *16p11.2*$^{df/+}$ mice display striking similarities with mouse models of glucose transporter-1 (GLUT-1) deficiency syndrome.[4,12–14] Despite these similarities, whether brain metabolism is altered in *16p11.2*$^{df/+}$ mice is still unknown, and the question remains whether 16p11.2-associated neurovascular alterations lead to changes in brain metabolism.

Growing evidence implicates metabolic contributions to the pathogenesis of ASD. It is generally accepted that these

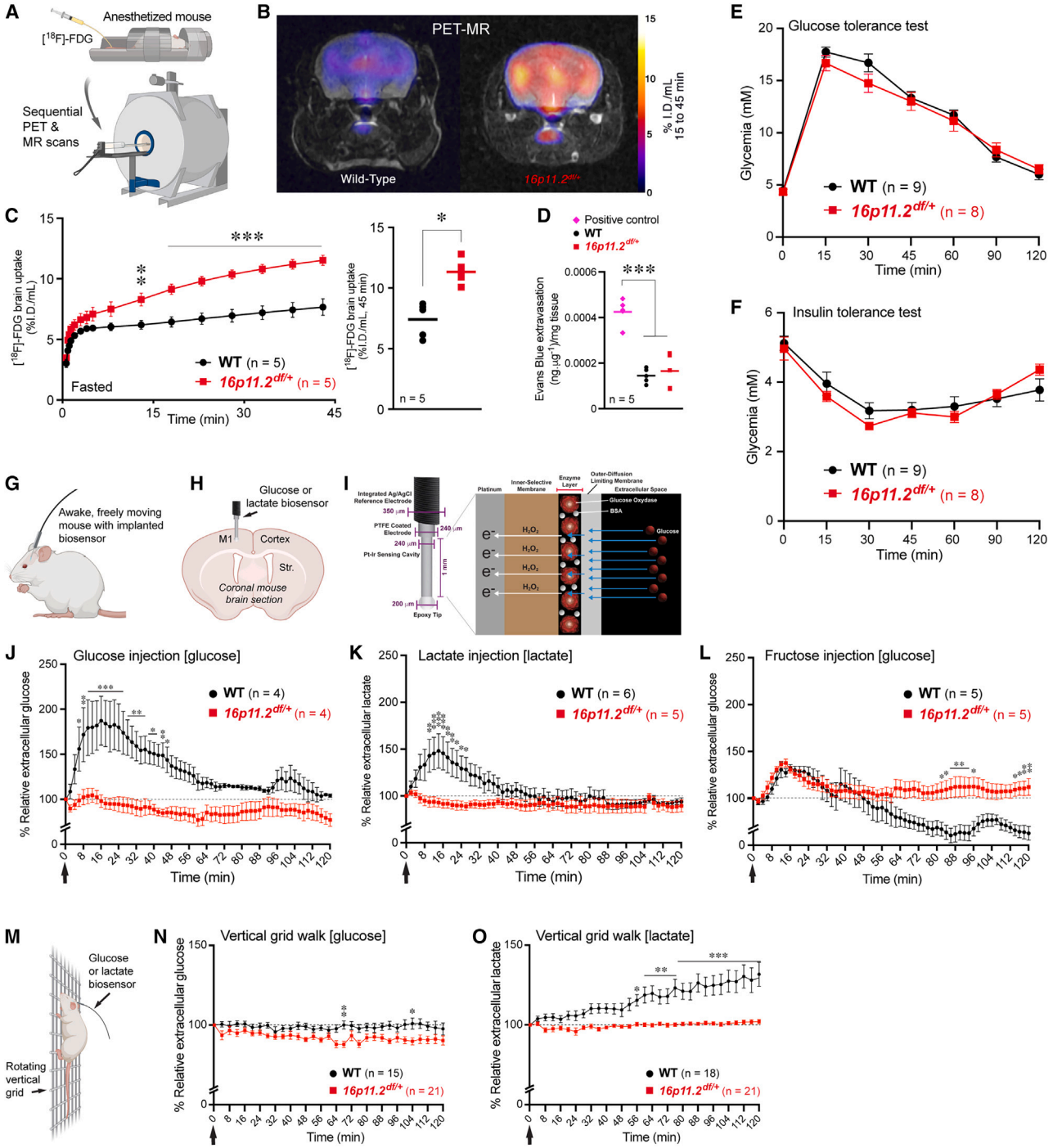

Figure 1. Brain-specific alteration of glucose metabolism in adult *16p11.2*$^{df/+}$ male mice

(A) Administration of [^{18}F]-2 fluoro-D-deoxyglucose (FDG) tracer using positron emission tomography (PET) superimposed with magnetic resonance imaging (MR).

(B) Representative PET-MR scans acquired between 15 and 45 min after tracer injection. I.D./mL, injected dose per mL of tissue.

(C) FDG uptake measured in fasted and anesthetized male *16p11.2*$^{df/+}$ (n = 5) and WT (n = 5) littermates.

(D) Quantification of microvascular integrity (Evans blue dye extravasation) in male *16p11.2*$^{df/+}$ (n = 5) and WT littermates (n = 5). Positive control: Evans blue dye extravasation 24 h after a photothrombotic stroke in adult male WT mice.

(E and F) Measurement of peripheral glycemia during a glucose tolerance test (E) or insulin tolerance test (F), with doses normalized to body weight, in *16p11.2*$^{df/+}$ (n = 8) and WT (n = 9) littermates.

(G) Illustration of an implanted biosensor for *in vivo* measurements of extracellular metabolites in the primary motor (M1) cortex of awake mice.

(legend continued on next page)

metabolic discrepancies in ASD relate to mitochondrial dysfunction,[15,16] and we have recently shown that *16p11.2*$^{df/+}$ mice display alterations in energy expenditure and concentration of plasma metabolites related to the mitochondrion.[17] While metabolic disturbances were also identified in the brain of ASD patients,[18–22] the cellular and molecular mechanisms underlying these alterations are unknown. Here, we investigated key metabolic players in the cerebral cortex of adult male *16p11.2*$^{df/+}$ mice that displayed significant neurovascular deficits compared with females[4] and their wild-type (WT) littermates in order to determine whether the previously observed neurovascular deficits are associated with and/or lead to changes in brain metabolism.

RESULTS

Anesthetized *16p11.2*$^{df/+}$ male mice display elevated brain glucose uptake

As glucose is a major fuel for brain cells, we first assessed glucose entry by means of positron emission tomography (PET) of [^{18}F]-2-fluorodeoxyglucose (FDG) uptake. FDG-PET signals revealed a significant increase in resting-state glucose uptake in the brain of anesthetized adult *16p11.2*$^{df/+}$ males compared with age-matched WT littermates (Figures 1A–1C). This phenotype appeared throughout the central nervous system (CNS) of mutant animals (Figure S1A) and was more pronounced in fasted mice (Figures 1C and S1B). Postmortem autoradiographs confirmed that increased FDG-PET signals were due to increased FDG accumulation in brain tissue (Figure S1C). Furthermore, increased parenchymal FDG was not attributed to compromised cerebrovascular permeability, as demonstrated by the absence of Evans blue dye leakage in *16p11.2*$^{df/+}$ mice (Figure 1D). As glucose is most efficiently used when it undergoes oxidative phosphorylation, we also assessed whether elevated glucose uptake in *16p11.2*$^{df/+}$ mice correlates with increased oxygen extraction/utilization. When quantifying cerebral blood oxygen saturation by photoacoustic imaging (Figures S1D–S1G and S2), we found no global difference in blood oxygen saturation between male *16p11.2*$^{df/+}$ and WT littermates, suggesting that increased oxidative phosphorylation may not drive elevated FDG-PET signals in *16p11.2*$^{df/+}$ male mice.

Awake 16p11.2$^{df/+}$ male mice display brain-specific alterations in glucose metabolism

To determine whether extracellular metabolite fluctuations are impacted by constitutive 16p11.2 (7qF3) haploinsufficiency, we measured extracellular glucose and lactate in the primary motor (M1) cortex of awake, freely moving adult male *16p11.2*$^{df/+}$ mice and WT littermates using electrochemical biosensors. We altered the systemic availability of different metabolites with various energy-producing capacities (i.e., glucose, lactate, fructose, and β-hydroxybutyrate [BHB]) through intraperitoneal (i.p.) injections and measured relative fluctuations of glucose and lactate in the extracellular space (Figures 1G–1L and S3D–S3H). Extracellular brain lactate was monitored in addition to glucose as a known by-product of glycolysis, which can be used as an indicator of non-oxidative glucose consumption.[23] We found that systemic glucose injection failed to induce the expected surge in relative extracellular glucose above baseline in *16p11.2*$^{df/+}$ mice (Figure 1J). Measurement of peripheral glucoregulatory responses in *16p11.2*$^{df/+}$ and WT mice via i.p. glucose and insulin tolerance tests (Figures 1E, 1F, and S3A–S3C) found no difference between genotypes, ruling out altered peripheral glucose availability as a root cause for the lack of net brain extracellular glucose increase in mutant mice. Growing evidence shows that the brain can meet a portion of its energetic needs by using alternative fuels such as ketone bodies or lactate, transported into the brain by the first isoform of the proton-coupled monocarboxylate transporter (MCT-1).[24] Here, we find that increases in systemic lactate, fructose, and BHB via i.p. injections are all capable of increasing extracellular brain glucose to comparable levels in *16p11.2*$^{df/+}$ mice and WT controls (Figures 1L, S3D, and S3F). However, 16p11.2 haploinsufficiency abolished the accumulation of extracellular brain lactate following an i.p. lactate injection (Figure 1K).

Finally, to assess whether extracellular glucose or lactate accumulation varied during physical activity (i.e., M1 cortex activation), mice underwent a behavioral task to activate the motor cortex[25] (Figure 1M). For both mutant and WT mice, extracellular glucose in M1 cortex remained relatively stable during this task (Figure 1N). However, only WT mice exhibited the expected rise in extracellular lactate, a normal consequence of neuronal activation[26,27] (Figure 1O).

Normal levels of transporters and canonical glycolytic pathways in the brain of male *16p11.2*$^{df/+}$ mice

One possible explanation for increased brain glucose uptake may be an elevated expression of cortical transporter proteins. Western blot measurements of cortical GLUT-1, GLUT-3, and MCT1 levels revealed no difference between *16p11.2*$^{df/+}$ mice and WT littermates (Figures S4A–S4C). Our previous mouse cerebral cortex endothelial cell RNA-seq database[4] also showed normal expression of endothelial *Scl2a1* (GLUT-1) and *Scl16a1*

(H) Location for biosensor implantation. Str., striatum; M1, primary motor cortex.
(I) Illustration depicting the enzyme-mediated process underlying biosensor electrode function.
(J) Measurement of extracellular glucose in M1 cortex following a 2-g/kg intraperitoneal (i.p.) injection of glucose in male *16p11.2*$^{df/+}$ (n = 4) and WT (n = 4) littermates.
(K) Measurements of extracellular lactate in M1 cortex following a 2-g/kg i.p. injection of lactate in male *16p11.2*$^{df/+}$ (n = 5) and WT (n = 6) littermates.
(L) Measurement of extracellular glucose in M1 cortex following a 2-g/kg i.p. injection of fructose in male *16p11.2*$^{df/+}$ (n = 5) and WT (n = 5) littermates.
(M) Depiction of a vertical climbing task for measuring relative fluctuations of extracellular glucose or lactate in activated M1 cortex.
(N) Measurements of extracellular glucose in M1 cortex during the vertical grid climbing task in *16p11.2*$^{df/+}$ (n = 21 trials) and WT (n = 15 trials) littermates.
(O) Measurements of extracellular lactate in M1 cortex during the same vertical grid climbing task in *16p11.2*$^{df/+}$ (n = 21 trials) and WT (n = 18 trials) littermates.
Data are mean ± SEM (C, left, and E–O) or mean with individual values (C, right, and D). *p < 0.05, **p < 0.01, ***p < 0.001 by a two-way repeated measure ANOVA and Sidak's *post hoc* test (C, left, and J–O), a one-way ANOVA and Tukey's *post hoc* test (D), or a two-tailed Mann-Whitney test (C, right). n = number of animals per group (A–L) or number of trials (N, O).

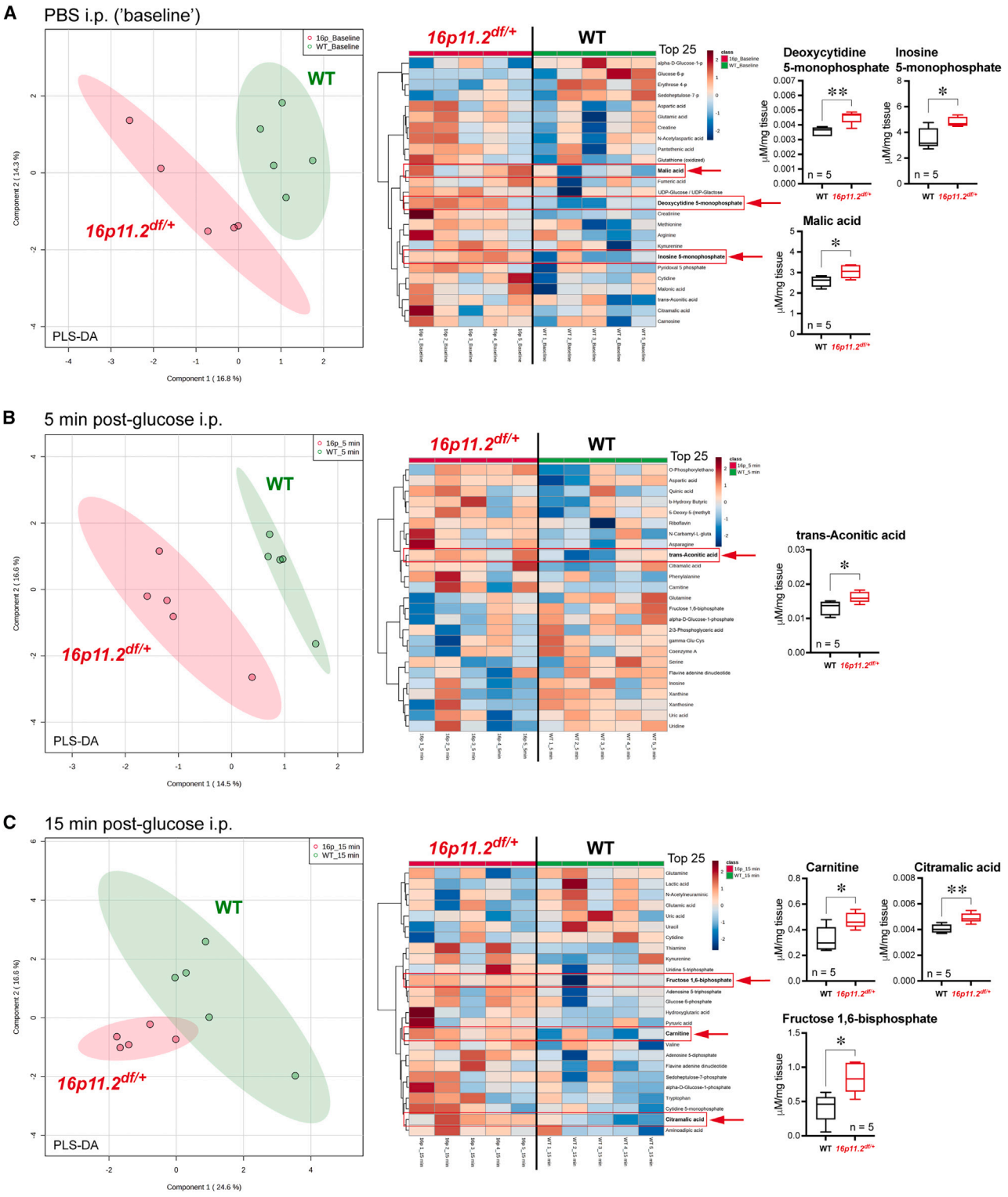

Figure 2. Enhanced metabolic response to peripheral glucose in the cerebral cortex of *16p11.2*$^{df/+}$ male mice

(A) Left: partial least-squares discriminant analysis (PLS-DA) of metabolomics data from cerebral cortex of *16p11.2*$^{df/+}$ (n = 5) and WT (n = 5) littermates 5 min after an intraperitoneal (i.p.) injection of 50 mM sterile phosphate buffer saline (PBS, "baseline"). Each data point represents one mouse. Middle: heatmap (multivariate statistical analysis) displaying the top 25 metabolites significantly altered by the genotype at baseline for all samples. Right: metabolites detected as most significantly altered by univariate statistical analysis.

(legend continued on next page)

(MCT-1) in *16p11.2*$^{df/+}$ mice (Figures S4A and S4C). Immunohistochemistry also revealed comparable levels of endothelial GLUT-1 in *16p11.2*$^{df/+}$ mice and WT littermates (Figure S4D). Thus, elevated glucose uptake and attenuated extracellular lactate response to an i.p. lactate injection in *16p11.2*$^{df/+}$ mice may not result from changes in transporter levels. Increased brain glucose uptake, unchanged transporter expression, and stable extracellular glucose pools suggest rapid glucose utilization in *16p11.2*$^{df/+}$ mice and/or saturated glucose transport at the blood-brain barrier. Stable blood oxygen saturation would indicate that glycolytic upregulation may be a likely mechanism supporting elevated glucose utilization. However, we find that protein levels of key enzymes involved in glycolysis are unchanged in the cerebral cortex of *16p11.2*$^{df/+}$ mice, including hexokinases 1 and 2, glycogen synthase kinase 3-beta (GSK3-β), as well as 5′ AMP-activated protein kinase (AMPK) and its phosphorylated form (Figure S4E).

Adult male 16p11.2$^{df/+}$ mice display enhanced metabolic responses to systemic glucose in the cerebral cortex

To better understand the kinetics of altered brain glucose metabolism in adult *16p11.2*$^{df/+}$ male mice following increases in systemic glucose, we performed targeted metabolomics on cerebral cortex extracts to assess changes in metabolite profiles after i.p. glucose injections. We matched the timing of metabolite extraction to the time course of extracellular glucose assessment (see Figure 1J), as follows: after a PBS injection (equivalent to baseline), 5 min after a glucose injection (rising slope), and 15 min after a glucose injection (maximal values preceding falling slope). Cortical metabolome of PBS-injected WT and *16p11.2*$^{df/+}$ littermates demonstrated distinct profiles, as shown by cluster separation of datasets by partial least-squares discriminant analysis (PLS-DA), confirming altered basal brain metabolism in *16p11.2*$^{df/+}$ mice compared with WT littermates (Figure 2A). From the top 25 altered metabolites (that include amino acids and nucleotides), deoxycytidine 5-monophosphate, inosine 5-monophosphate, and malic acid were found to be most significantly increased in *16p11.2*$^{df/+}$ compared with WT mice, indicative of changes in DNA biosynthesis, purine metabolism, and TCA cycle (Figure 2A). Metabolites measured 5 min (Figures 2B) and 15 min (Figure 2C) after i.p. glucose injection also demonstrated distinct profiles between *16p11.2*$^{df/+}$ and WT littermates (see also Figure S5). Overall, peripheral glucose injections in *16p11.2*$^{df/+}$mice resulted in increased abundance of metabolites involved in energy metabolism, including *trans*-aconitic acid, an intermediate metabolite in the TCA cycle; carnitine, required for energy production and fatty acid metabolism; citramalic acid, involved in pyruvate metabolism; and fructose 1,6-biphosphate, a high-energy intermediate of glycolysis (Figures 2B and 2C). These metabolite alterations differ from those found at baseline (Figure 2A), supporting our evidence of increased brain glucose metabolic rates in *16p11.2*$^{df/+}$ mice. We also identified time-dependent changes in metabolic responses to increased systemic glucose availability between WT and *16p11.2*$^{df/+}$ mice (Figures 3 andS5). In particular, time course heat maps for either group averages (Figure 3A) illustrate distinct dynamic responses to glucose availability between genotypes. Altogether, these findings demonstrate that *16p11.2*$^{df/+}$ mice display a shift in brain glucose metabolism, which varies in function of glucose availability.

Endothelial-specific 16p11.2 haploinsufficiency leads to elevated brain glucose uptake

Our previous work demonstrated that endothelium-specific 16p11.2 deletion (*16p11.2*$^{\Delta EC}$ mice) partially recapitulated neurovascular and behavioral abnormalities observed in constitutive *16p11.2*$^{df/+}$ mutants.[4] Therefore, we opted to look more closely at the role of the endothelium in 16p11.2 deletion-induced metabolic dysregulation. Similar to anesthetized *16p11.2*$^{df/+}$ male mice, *16p11.2*$^{\Delta EC}$ males displayed a significant increase in resting-state brain FDG uptake compared with age-matched *Cdh5-Cre*$^{tg/+}$ control littermates (Figure 4A). This phenotype also appeared throughout the CNS of mutant animals (Figure 4B). These data demonstrate that endothelial 16p11.2 deficiency is sufficient to drive a CNS-wide increase in glucose uptake.

Brain endothelial cells from adult *16p11.2*$^{df/+}$ male mice possess fewer mitochondria

The observations above led us to test whether the metabolic machinery is altered in brain endothelial cells from constitutive *16p11.2*$^{df/+}$ mutants *in vivo*. Analysis of transmission electron micrographs revealed a significant reduction in the number of mitochondria within brain capillary endothelial cells (Figure 4C), but not in surrounding astrocytic endfeet (Figure S6A), in *16p11.2*$^{df/+}$ mice compared with WT littermates. There was, however, no impact of the 16p11.2 deletion on mitochondria ultrastructure (Figure 4C). Fewer endothelial mitochondria in *16p11.2*$^{df/+}$ mice may imply a reduced capacity for oxidative phosphorylation, further supporting that the observed metabolic changes are unlikely to stem from elevated oxidative phosphorylation/mitochondrial glucose use. To assess whether reduced mitochondria number in *16p11.2*$^{df/+}$ brain endothelial cells was caused by altered mitochondria dynamics, we measured protein levels of key regulators of mitochondria fusion and fission, including optic atrophy 1 (OPA1), dynamin-related protein 1 (DRP1), and mitofusins 1 and 2 (MFN1, MFN2). None of these proteins appeared altered in *16p11.2*$^{df/+}$ brain endothelial cells (Figures 4D and S6B). To test the possibility of dysregulated mitochondrial biogenesis in *16p11.2*$^{df/+}$ brain endothelial cells, we quantified protein levels of the nuclear transcription factor

(B) Left: PLS-DA of metabolomics data from cerebral cortex of *16p11.2*$^{df/+}$ (n = 5) and WT (n = 5) littermates 5 min after a 2-g/kg i.p. glucose injection. Each data point represents one mouse. Middle: heatmap (multivariate statistical analysis) displaying the top 25 metabolites significantly altered by the genotype 5 min after glucose administration for all samples. Right: metabolites detected as most significantly altered by univariate statistical analysis.
(C) Left: PLS-DA of metabolomics data from the cerebral cortex of *16p11.2*$^{df/+}$ (n = 5) and WT (n = 5) littermates 15 min after a 2-g/kg i.p. glucose injection. Each data point represents one mouse. Middle: heatmap (multivariate statistical analysis) displaying the top 25 metabolites significantly altered by the genotype 15 min after glucose administration for all samples. Right: metabolites detected as most significantly altered by univariate statistical analysis. Data in rightmost panels are whisker boxes (min to max, center line indicating median). *p < 0.05, **p < 0.01 by a two-tailed unpaired t test. n = number of animals per group.

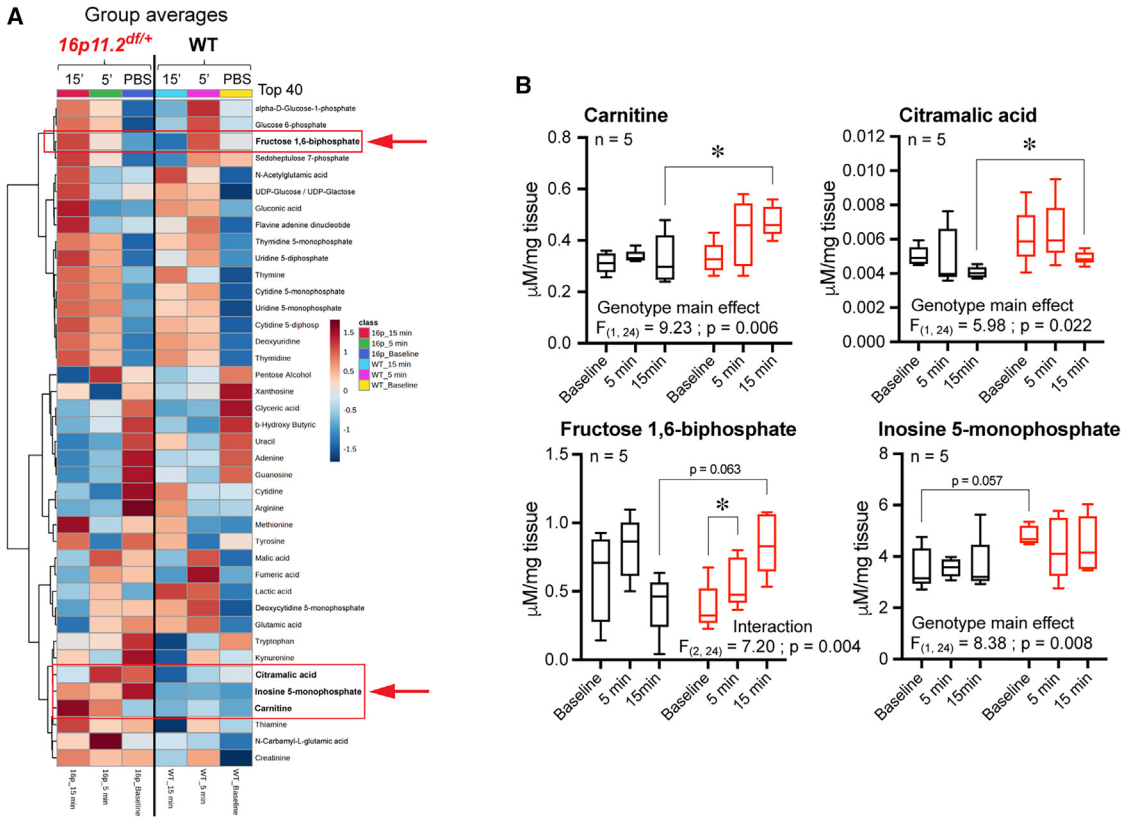

Figure 3. Time course of cerebral metabolic response to peripheral glucose in *16p11.2*$^{df/+}$ and WT male mice

(A) Heatmap (multivariate statistical analysis) displaying group averages for the top 40 metabolites significantly altered by genotype and/or glucose administration.

(B) Metabolites detected as most significantly altered by multivariate statistical analysis. Data in (B) are whisker boxes (min to max, center line indicating median). *p < 0.05 by two-way ANOVA and Tukey's *post hoc* test. n = number of animals per group.

peroxisome proliferator-activated receptor gamma coactivator 1-alpha (PGC-1α), as well as its truncated splicing variant N-terminal (NT)-PGC-1α, which orchestrate the expression of genes involved in mitochondrial biogenesis by activating additional transcription factors.[28] While protein levels of PGC-1α did not appear significantly reduced in *16p11.2*$^{df/+}$ brain endothelial cells compared with WT cells (Figure S6C), a most striking finding was the absence of NT-PGC-1α in 16p11.2-deficient brain endothelial cells (Figures 4E and S6D). These data suggest impaired mitochondrial biogenesis as a potential source of reduced mitochondria number and ensuing endothelial dysfunction in *16p11.2*$^{df/+}$ mice.

DISCUSSION

Here, we demonstrate that glucose uptake was increased in a mouse model of the 16p11.2 deletion syndrome. While FDG uptake has been shown to mostly depend on astrocytes,[29–31] we have previously shown that, at least structurally, astroglial and microglial lineages develop normally in *16p11.2*$^{df/+}$ mice.[4] In addition, we provide evidence of normal mitochondria in astrocytic endfeet of *16p11.2*$^{df/+}$ mice. Increased brain glucose transport, measured by FDG, has also been demonstrated in a mouse model of GLUT1 deficiency.[12] In this GLUT1 deficiency model, glucose influx into the brain was expectedly reduced, but intracellular phosphorylation was increased, resulting in elevated deoxyglucose accumulation.[12] Thus, this demonstrates a means by which brain glucose uptake can take place without proportionate increases in transport.[32] Despite all the normal parameters observed in the 16p11.2-haplodeficient mice (e.g., oxygen extraction, transporters, permeability, hexokinase), elevating blood glucose concentration did not result in net elevations of extracellular brain glucose in 16p11.2-haplodeficient mice, suggesting that glucose transport is saturated in order to meet heightened brain glucose use through non-oxidative pathways. Elevated extracellular glucose following systemic injections of lactate, fructose, and BHB further supports the notion of saturated vascular glucose transport as these substrates enter the brain through alternative transports (MCT1 and GLUT5) and, as alternative fuels, can spare glucose use.[33–36]

In line with previous reports of mitochondrial dysregulation in neurodevelopmental disorders, including ASD,[37,38] we have demonstrated a decreased mitochondria number in 16p11.2-deficient capillary endothelial cells, consistent with absence of transcription factor NT- PGC1α regulating mitochondrial biogenesis. This finding is particularly interesting considering that

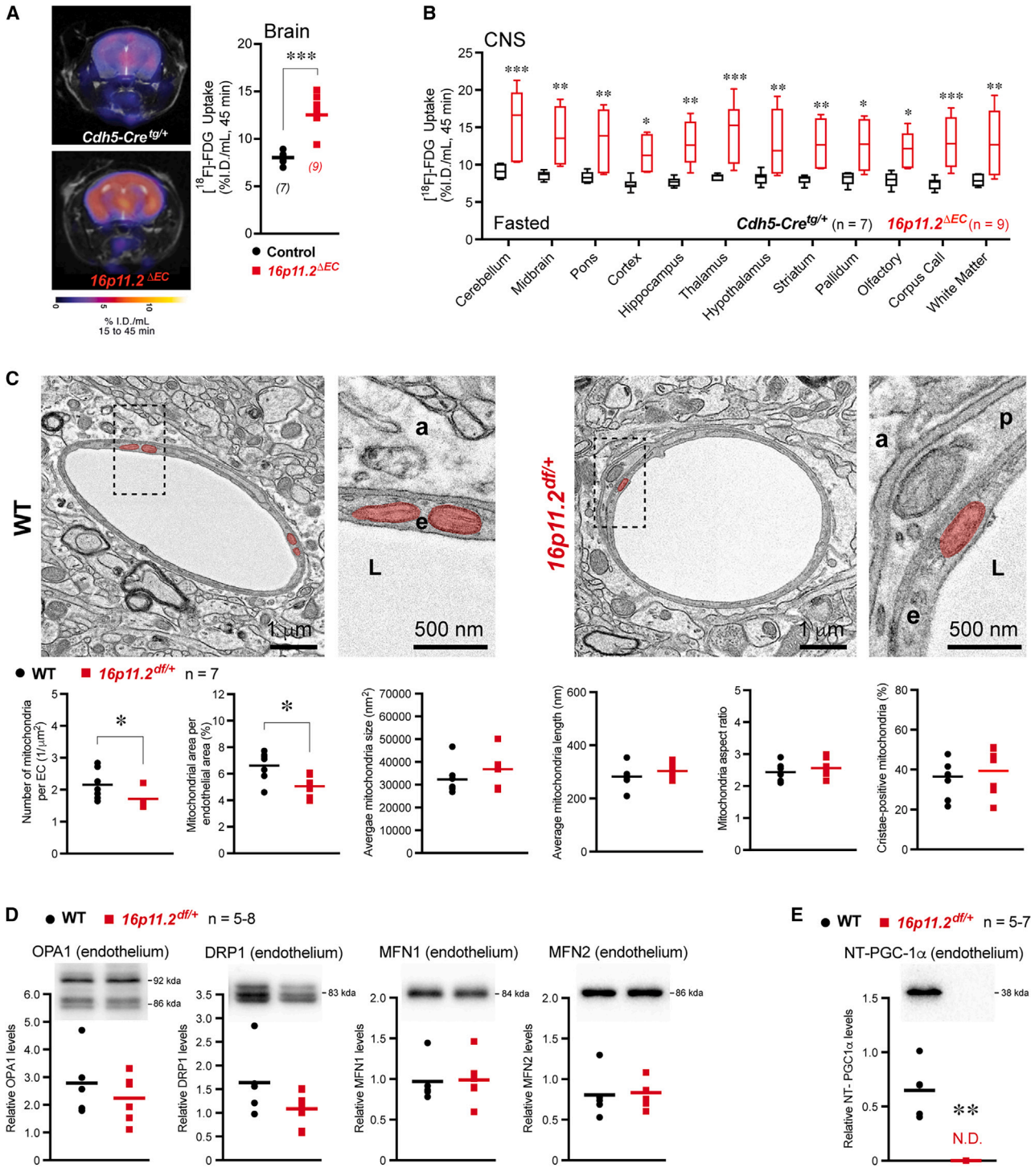

Figure 4. Reduced mitochondrial number in 16p11.2-deficient brain endothelial cells

(A) Left: representative image of positron emission tomography-magnetic resonance imaging (PET-MR). FDG, [^{18}F]-2 fluoro-D-deoxyglucose; I.D./mL, injected dose per mL of tissue. Right: acute brain FDG uptake quantified by PET imaging 45 min after tracer injection in the brain of fasted, anesthetized male mice with endothelium-specific 16p11.2 deletion (*16p11.2$^{\Delta EC}$*, n = 9) and control littermates (*Cdh5-Cre$^{tg/+}$*, n = 7).

(B) Acute regional FDG uptake quantified by PET-MR imaging 45 min after tracer injection in the central nervous system (CNS) of fasted, anesthetized male *16p11.2$^{\Delta EC}$* mice (n = 9) and control littermates (n = 7).

(legend continued on next page)

endothelial-specific 16p11.2 deletion recapitulates many of the observations made with constitutive 16p11.2 haplodeficiency, including cerebrovascular and behavioral abnormalities.[4] Since endothelial cells are glycolytic,[39–41] the energy-producing capacity of endothelial mitochondria is secondary to its signaling properties in maintaining proper health and function, such as vasodilation,[41,42] blood-brain barrier integrity,[43,44] and endothelial proliferation.[39]

Neuronal activation, including during behavior, increases extracellular lactate through what is thought to be a glycolysis-[45] or glycogen-dependent[46] process. Here, 16p11.2 haplodeficiency abolished this behavior-induced rise in extracellular lactate in M1 cortex, suggesting reduced glycolytic capacity. This is in contrast to multiple reports of increased glycolysis in ASD[47,48] and our observation of elevated inosine 5-monophosphate, which has been associated with elevated glycolysis in rabbit heart.[49] Shortly after the metabolic challenge (glucose injection), *trans*-aconitic acid was upregulated in the cerebral cortex of *16p11.2*$^{df/+}$ mice, which may have inhibited oxidative phosphorylation (OXPHOS).[50] Subsequently, carnitine and fructose 1,6-bisphosphate were upregulated. Carnitine is essential for long-chain Acyl-CoA transport into the mitochondria and thus beta-oxidation, likely representing an increase in fatty acid oxidation.[51] Moreover, trends toward increased p-AMPK/AMPK ratios may indicate a subtle reduction in glycogen production[52] and a shift toward β-oxidation,[53] respectively. Fructose 1,6-bisphosphate is capable of both reducing neuronal excitability[54] and shifting glycolytic products away from OXPHOS and toward the pentose phosphate pathway (PPP).[55] The results further nuance the altered metabolic profile of the ASD model, suggesting a shift away from glucose-centric ATP-producing pathways toward lipid metabolism and shunting of glucose toward the PPP. The PPP uses glucose to maintain antioxidant capacity in cells.[56] Enhanced processing of glucose through the PPP may be required in *16p11.2*$^{df/+}$ mice to compensate for enhanced ROS production that accompanies the often-observed dysfunctional mitochondria.[48,57,58] Given that the PPP is not an oxygen-dependent pathway, shunting additional glucose taken up by the *16p11.2*$^{df/+}$ mouse brain toward this pathway may provide an explanation for both comparable oxygen saturation and elevated glucose uptake.

Altogether, we raise the question of how additional glucose taken up by the brain is metabolized and for what purpose. Our findings show that constitutive 16p11.2 (7qF3) hemizygosity leads to a shift in brain glucose metabolism. We propose a new model whereby *16p11.2*$^{df/+}$ male mice modulate their glycolytic pathway to shunt additional glucose toward the PPP caused by dysfunctional endothelial cells that possess fewer mitochondria. Consistent with observations of dysregulated signaling, hypermetabolism, and benefits of altered diets in ASD,[59,60] this model suggests that the resulting energy deficit is mediated by increased mitochondrial fatty acid oxidation to meet the brain's elevated energetic demands. However, alternative possibilities cannot be ruled out. During development, glycolysis is increased in correlation with moments of high synaptic growth. Lactate (a glycolytic by-product) has been shown to act as a signaling molecule capable of potentiating angiogenesis and neurogenesis[61] as well as regulate neuronal activity[62–64] and synaptic plasticity.[65,66] Recent hypotheses suggest a main function of glycolysis, and its by-products, is to support biosynthesis.[67–70] Therefore, altered glycolysis may represent an energetic adaptation to deficient mitochondria or a biosynthetic compensatory mechanism to support the additional bioinfrastructure required due to unregulated growth within the ASD brain. Future work may wish to investigate mechanisms underlying the metabolic dysfunction induced by this mutation and the dependence of these dysregulations on endothelial dysfunction with respect to ROS production and the PPP.

Limitations of the study

The results presented herein lead us to hypothesize a causal relationship between endothelial abnormalities and CNS-wide altered metabolic profile in *16p11.2*$^{df/+}$ male mice. This hypothesis is, however, based on assumptions that should be verified in future work. The tools and methods enabled inferences regarding the impact of this mutation on metabolic pathways, which will need to be confirmed with more direct measures. Chiefly, we recognize that measures of protein expression do not equate enzymatic or transporter activity and acknowledge that the methodologies used (e.g., FDG-PET scans, biosensors, photoacoustic imaging, metabolomics) to infer activity of various metabolic pathways (OXPHOS, glycolysis, PPP) provide an incomplete snapshot. Biosensors measure net fluxes of metabolites without representing the various influxes and effluxes; the metabolomics and measures of protein expression are not specific to cellular or sub-cellular compartments. Future studies may wish to include measures of mitochondrial respiration that enable the location of dysfunction, if any, at specific complexes (e.g., inhibition of complex II by oxaloacetate), as well as measure direct oxygen use and energy production. Nuclear magnetic resonance spectrometry coupled with ^{13}C-labeled glucose would allow for a more comprehensive understanding of substrate fate through the complementary pathways discussed (glycolysis, OXPHOS, PPP). Finally, this work focuses on the *metabolic* contributions of these substrates to the observed results. However, it does not assess or disentangle the impact that these substrates have on other processes through their signaling properties (e.g., effect of lactate on neuronal activity).

(C) Top panels: representative images of mitochondrial structure assessment in cortical capillaries from WT or mutant mice by transmission electron microscopy. a, astrocyte; e, endothelium; L, lumen; p, pericyte. For clarity, endothelial mitochondria were pseudocolored in red. Bottom graphs: quantitative assessment of mitochondria structure in cortical endothelial cells from *16p11.2*$^{df/+}$ mice (n = 7) compared with WT littermates (n = 7).

(D) Western blot quantification of relative levels of proteins associated with mitochondria fusion or fission (OPA-1, DRP1, and MFN1 and -2) in primary mouse brain endothelial cells (n = 5–7) isolated from male *16p11.2*$^{df/+}$ and WT littermates.

(E) Western blot quantification of relative N-terminal (NT)-PGC-1α protein levels in primary brain endothelial cells from male *16p11.2*$^{df/+}$ (n = 7) and WT (n = 5) littermates. N.D., not detected. Data are mean with individual values (A, C–E) or whisker boxes in (B) (min to max, center line indicating median). *p < 0.05, **p < 0.01, ***p < 0.001 by a two-tailed Mann-Whitney test (A, C–E) or a two-way ANOVA and Tukey's *post hoc* test (B). n = number of animals per group.

Despite these limitations, we provide initial evidence of an altered CNS metabolic profile in a mouse model of a common mutation linked to ASD.

STAR★METHODS

Detailed methods are provided in the online version of this paper and include the following:

- KEY RESOURCES TABLE
- RESOURCE AVAILABILITY
  - Lead contact
  - Materials availability
  - Data and code availability
- EXPERIMENTAL MODEL AND SUBJECT DETAILS
  - Mouse husbandry
  - Genotyping
- METHOD DETAILS
  - FDG-PET scan
  - Extracellular brain glucose and lactate measurements
  - Photoacoustic imaging
  - Peripheral measurements of glucose metabolism
  - Western blot on cerebral cortex or brain endothelial cell lysates
  - Immunofluorescence
  - Systemic glucose injections and tissue collection for metabolomics
  - Targeted metabolomics
  - Transmission electron microscopy (TEM)
  - Photothrombotic (PT) stroke and Evans blue dye (EBD) leakage assay
- QUANTIFICATION AND STATISTICAL ANALYSIS

SUPPLEMENTAL INFORMATION

Supplemental information can be found online at https://doi.org/10.1016/j.celrep.2023.112485.

ACKNOWLEDGMENTS

We thank Carlie Boisvert (Lacoste lab) for technical assistance and Andrew Heinmiller (Fujifilm VisualSonics) for guidance on photoacoustic imaging. We thank the CRCHUM rodent metabolic phenotyping core facility for their help with tolerance tests. Metabolites were analyzed at the University of Ottawa Metabolomics Core Facility; this facility is supported by the Terry Fox Foundation and Ottawa University. B.L. was supported by start-up funds from the Ottawa Hospital Research Institute, a Canadian Institutes of Health Research (grant #388805), an award from The Scottish Rite Charitable Foundation of Canada (grant #17112), and a *J.P. Bickell Foundation* medical research grant. Part of this work is also funded by an Autism Research Program Idea Development Award from the US Department of Defense office of the Congressionally Directed Medical Research Programs (grant #AR210134). C.M. was supported by the Natural Sciences and Engineering Council of Canada (grant #RGPIN 2019-03945) and by an equipment grant from the Canadian Foundation for Innovation and the Ontario Research Fund. T.A. was supported by a salary award from Fonds de Recherche du Québec – Santé (FRQS). M.C. is supported by a doctoral training award from the FRQS. J.O. is supported by a doctoral training award from CIHR. P.K. is supported by a doctoral training award from uOBMRI. A.J.S. thanks the Canada Research Chairs program (950-230754), the Canadian Foundation for Innovation - John Evans Leadership Fund, and NSERC (grant RGPIN 2015-05796).

AUTHOR CONTRIBUTIONS

A.B., A.K., Y.T., J.O., S.Y., K.B., C.P., S.N., P.K., M.Y., T.A., and A.J.S. performed experiments. M.C. and M.-K.St.-P. provided technical support for transmission electron microscopy tissue processing. A.B., J.O., S.Y., K.B., C.P., S.N., P.K., M.Y., T.A., and A.J.S. analyzed data. B.L. conceived and led the project. A.B. and B.L. wrote the manuscript with input from all co-authors.

DECLARATION OF INTERESTS

The authors declare no competing interests.

Received: March 8, 2022
Revised: February 20, 2023
Accepted: April 22, 2023
Published: May 6, 2023

REFERENCES

1. Andreone, B.J., Lacoste, B., and Gu, C. (2015). Neuronal and vascular interactions. Annu. Rev. Neurosci. *38*, 25–46.
2. Sonnay, S., Gruetter, R., and Duarte, J.M.N. (2017). How energy metabolism supports cerebral function: insights from (13)C magnetic resonance studies in vivo. Front. Neurosci. *11*, 288.
3. Carmeliet, P., and Jain, R.K. (2011). Molecular mechanisms and clinical applications of angiogenesis. Nature *473*, 298–307.
4. Ouellette, J., Toussay, X., Comin, C.H., Costa, L.d.F., Ho, M., Lacalle-Aurioles, M., Freitas-Andrade, M., Liu, Q.Y., Leclerc, S., Pan, Y., et al. (2020). Vascular contributions to 16p11.2 deletion autism syndrome modeled in mice. Nat. Neurosci. *23*, 1090–1101.
5. Rylaarsdam, L., and Guemez-Gamboa, A. (2019). Genetic causes and modifiers of autism spectrum disorder. Front. Cell. Neurosci. *13*, 385.
6. Kumar, R.A., KaraMohamed, S., Sudi, J., Conrad, D.F., Brune, C., Badner, J.A., Gilliam, T.C., Nowak, N.J., Cook, E.H., Jr., Dobyns, W.B., and Christian, S.L. (2008). Recurrent 16p11.2 microdeletions in autism. Hum. Mol. Genet. *17*, 628–638.
7. Weiss, L.A., Shen, Y., Korn, J.M., Arking, D.E., Miller, D.T., Fossdal, R., Saemundsen, E., Stefansson, H., Ferreira, M.A.R., Green, T., et al. (2008). Association between microdeletion and microduplication at 16p11.2 and autism. N. Engl. J. Med. *358*, 667–675.
8. Steinberg, S., de Jong, S., Mattheisen, M., Costas, J., Demontis, D., Jamain, S., Pietiläinen, O.P.H., Lin, K., Papiol, S., Huttenlocher, J., et al. (2014). Common variant at 16p11.2 conferring risk of psychosis. Mol. Psychiatr. *19*, 108–114.
9. Andrikopoulos, P., Eccles, S.A., and Yaqoob, M.M. (2017). Coupling between the TRPC3 ion channel and the NCX1 transporter contributed to VEGF-induced ERK1/2 activation and angiogenesis in human primary endothelial cells. Cell. Signal. *37*, 12–30.
10. Smits, M., Wurdinger, T., van het Hof, B., Drexhage, J.A.R., Geerts, D., Wesseling, P., Noske, D.P., Vandertop, W.P., de Vries, H.E., and Reijerkerk, A. (2012). Myc-associated zinc finger protein (MAZ) is regulated by miR-125b and mediates VEGF-induced angiogenesis in glioblastoma. Faseb. J. *26*, 2639–2647.
11. Yu, Z., Zhang, T., Gong, C., Sheng, Y., Lu, B., Zhou, L., Ji, L., and Wang, Z. (2016). Erianin inhibits high glucose-induced retinal angiogenesis via blocking ERK1/2-regulated HIF-1alpha-VEGF/VEGFR2 signaling pathway. Sci. Rep. *6*, 34306.
12. Furuse, T., Mizuma, H., Hirose, Y., Kushida, T., Yamada, I., Miura, I., Masuya, H., Funato, H., Yanagisawa, M., Onoe, H., and Wakana, S. (2019). A new mouse model of GLUT1 deficiency syndrome exhibits abnormal sleep-wake patterns and alterations of glucose kinetics in the brain. Dis. Model. Mech. *12*, dmm038828.

13. Veys, K., Fan, Z., Ghobrial, M., Bouché, A., García-Caballero, M., Vriens, K., Conchinha, N.V., Seuwen, A., Schlegel, F., Gorski, T., et al. (2020). Role of the GLUT1 glucose transporter in postnatal CNS angiogenesis and blood-brain barrier integrity. Circ. Res. *127*, 466–482.

14. Tang, M., Park, S.H., Petri, S., Yu, H., Rueda, C.B., Abel, E.D., Kim, C.Y., Hillman, E.M., Li, F., Lee, Y., et al. (2021). An early endothelial cell-specific requirement for Glut1 is revealed in Glut1 deficiency syndrome model mice. JCI Insight *6*, e145789.

15. Citrigno, L., Muglia, M., Qualtieri, A., Spadafora, P., Cavalcanti, F., Pioggia, G., and Cerasa, A. (2020). The mitochondrial dysfunction hypothesis in autism spectrum disorders: current status and future perspectives. Int. J. Mol. Sci. *21*, 5785.

16. Frye, R.E., Cakir, J., Rose, S., Palmer, R.F., Austin, C., Curtin, P., and Arora, M. (2021). Mitochondria may mediate prenatal environmental influences in autism spectrum disorder. J. Personalized Med. *11*, 218.

17. Menzies, C., Naz, S., Patten, D., Alquier, T., Bennett, B.M., and Lacoste, B. (2021). Distinct basal metabolism in three mouse models of neurodevelopmental disorders. eNeuro *8*. ENEURO.0292-20.2021.

18. Anil Kumar, B.N., Malhotra, S., Bhattacharya, A., Grover, S., and Batra, Y.K. (2017). Regional cerebral glucose metabolism and its association with phenotype and cognitive functioning in patients with autism. Indian J. Psychol. Med. *39*, 262–270.

19. Cheng, N., Rho, J.M., and Masino, S.A. (2017). Metabolic dysfunction underlying autism spectrum disorder and potential treatment approaches. Front. Mol. Neurosci. *10*, 34.

20. Gu, F., Chauhan, V., Kaur, K., Brown, W.T., LaFauci, G., Wegiel, J., and Chauhan, A. (2013). Alterations in mitochondrial DNA copy number and the activities of electron transport chain complexes and pyruvate dehydrogenase in the frontal cortex from subjects with autism. Transl. Psychiatry *3*, e299.

21. Jann, K., Hernandez, L.M., Beck-Pancer, D., McCarron, R., Smith, R.X., Dapretto, M., and Wang, D.J.J. (2015). Altered resting perfusion and functional connectivity of default mode network in youth with autism spectrum disorder. Brain Behav. *5*, e00358.

22. Rossignol, D.A., and Frye, R.E. (2012). Mitochondrial dysfunction in autism spectrum disorders: a systematic review and meta-analysis. Mol. Psychiatr. *17*, 290–314.

23. Kiyatkin, E.A., and Lenoir, M. (2012). Rapid fluctuations in extracellular brain glucose levels induced by natural arousing stimuli and intravenous cocaine: fueling the brain during neural activation. J. Neurophysiol. *108*, 1669–1684.

24. Jensen, N.J., Wodschow, H.Z., Nilsson, M., and Rungby, J. (2020). Effects of ketone bodies on brain metabolism and function in neurodegenerative diseases. Int. J. Mol. Sci. *21*, 8767.

25. Béland-Millar, A., and Messier, C. (2022). Voluntary behavior and training conditions modulate in vivo extracellular glucose and lactate in the mouse primary motor cortex. Front. Neurosci. *15*, 732242.

26. Béland-Millar, A., and Messier, C. (2018). Fluctuations of extracellular glucose and lactate in the mouse primary visual cortex during visual stimulation. Behav. Brain Res. *344*, 91–102.

27. Dienel, G.A., and Hertz, L. (2001). Glucose and lactate metabolism during brain activation. J. Neurosci. Res. *66*, 824–838.

28. Chang, J.S., Ghosh, S., Newman, S., and Salbaum, J.M. (2018). A map of the PGC-1α- and NT-PGC-1α-regulated transcriptional network in brown adipose tissue. Sci. Rep. *8*, 7876.

29. Zimmer, E.R., Parent, M.J., Souza, D.G., Leuzy, A., Lecrux, C., Kim, H.I., Gauthier, S., Pellerin, L., Hamel, E., and Rosa-Neto, P. (2017). [^{18}F]FDG PET signal is driven by astroglial glutamate transport. Nat. Neurosci. *20*, 393–395.

30. Zimmer, E.R., Pascoal, T.A., Rosa-Neto, P., Nordberg, A., and Pellerin, L. (2022). Comment on « Microglial activation states drive glucose uptake and FDG-PET alterations in neurodegenerative diseases. Sci. Transl. Med. *14*, eabm8302.

31. Rocha, A., Bellaver, B., Souza, D.G., Schu, G., Fontana, I.C., Venturin, G.T., Greggio, S., Fontella, F.U., Schiavenin, M.L., Machado, L.S., et al. (2022). Clozapine induces astrocyte-dependent FDG-PET hypometabolism. Eur. J. Nucl. Med. Mol. Imag. *49*, 2251–2264.

32. Leybaert, L., De Bock, M., Van Moorhem, M., Decrock, E., and De Vuyst, E. (2007). Neurobarrier coupling in the brain: adjusting glucose entry with demand. J. Neurosci. Res. *85*, 3213–3220.

33. Svart, M., Gormsen, L.C., Hansen, J., Zeidler, D., Gejl, M., Vang, K., Aanerud, J., and Moeller, N. (2018). Regional cerebral effects of ketone body infusion with 3-hydroxybutyrate in humans: reduced glucose uptake, unchanged oxygen consumption and increased blood flow by positron emission tomography. A randomized, controlled trial. PLoS One *13*, e0190556.

34. LaManna, J.C., Salem, N., Puchowicz, M., Erokwu, B., Koppaka, S., Flask, C., and Lee, Z. (2009). Ketones suppress brain glucose consumption. Adv. Exp. Med. Biol. *645*, 301–306.

35. van Hall, G., Strømstad, M., Rasmussen, P., Jans, O., Zaar, M., Gam, C., Quistorff, B., Secher, N.H., and Nielsen, H.B. (2009). Blood lactate is an important energy source for the human brain. J. Cerebr. Blood Flow Metabol. *29*, 1121–1129.

36. Wyss, M.T., Jolivet, R., Buck, A., Magistretti, P.J., and Weber, B. (2011). In vivo evidence for lactate as a neuronal energy source. J. Neurosci. *31*, 7477–7485.

37. Graham, S.F., Turkoglu, O., Yilmaz, A., Ustun, I., Ugur, Z., Bjorndhal, T., Han, B., Mandal, R., Wishart, D., and Bahado-Singh, R.O. (2020). Targeted metabolomics highlights perturbed metabolism in the brain of autism spectrum disorder sufferers. Metabolomics *16*, 59.

38. Yardeni, T., Cristancho, A.G., McCoy, A.J., Schaefer, P.M., McManus, M.J., Marsh, E.D., and Wallace, D.C. (2021). An mtDNA mutant mouse demonstrates that mitochondrial deficiency can result in autism endophenotypes. Proc. Natl. Acad. Sci. USA *118*. e2021429118.

39. Leung, S.W.S., and Shi, Y. (2022). The glycolytic process in endothelial cells and its implications. Acta Pharmacol. Sin. *43*, 251–259.

40. Groschner, L.N., Waldeck-Weiermair, M., Malli, R., and Graier, W.F. (2012). Endothelial mitochondria–less respiration, more integration. Pflügers Archiv *464*, 63–76.

41. Eelen, G., de Zeeuw, P., Simons, M., and Carmeliet, P. (2015). Endothelial cell metabolism in normal and diseased vasculature. Circ. Res. *116*, 1231–1244.

42. Gladwin, M.T., and Shiva, S. (2009). The ligand binding battle at cytochrome c oxidase: how NO regulates oxygen gradients in tissue. Circ. Res. *104*, 1136–1138.

43. Doll, D.N., Hu, H., Sun, J., Lewis, S.E., Simpkins, J.W., and Ren, X. (2015). Mitochondrial crisis in cerebrovascular endothelial cells opens the blood-brain barrier. Stroke *46*, 1681–1689.

44. Eelen, G., de Zeeuw, P., Treps, L., Harjes, U., Wong, B.W., and Carmeliet, P. (2018). Endothelial cell metabolism. Physiol. Rev. *98*, 3–58.

45. Pellerin, L., and Magistretti, P.J. (1994). Glutamate uptake into astrocytes stimulates aerobic glycolysis: a mechanism coupling neuronal activity to glucose utilization. Proc. Natl. Acad. Sci. USA *91*, 10625–10629.

46. Newman, L.A., Korol, D.L., and Gold, P.E. (2011). Lactate produced by glycogenolysis in astrocytes regulates memory processing. PLoS One *6*, e28427.

47. Pecorelli, A., Ferrara, F., Messano, N., Cordone, V., Schiavone, M.L., Cervellati, F., Woodby, B., Cervellati, C., Hayek, J., and Valacchi, G. (2020). Alterations of mitochondrial bioenergetics, dynamics, and morphology support the theory of oxidative damage involvement in autism spectrum disorder. Faseb. J. *34*, 6521–6538.

48. Rose, S., Bennuri, S.C., Wynne, R., Melnyk, S., James, S.J., and Frye, R.E. (2017). Mitochondrial and redox abnormalities in autism lymphoblastoid cells: a sibling control study. Faseb. J. *31*, 904–909.

49. Lewandowski, E.D., Johnston, D.L., and Roberts, R. (1991). Effects of inosine on glycolysis and contracture during myocardial ischemia. Circ. Res. *68*, 578–587.

50. Weinhouse, S., millington, R.H., and Wenner, C.E. (1951). Metabolism of neoplastic tissue. I. The oxidation of carbohydrate and fatty acids in transplanted tumors. Cancer Res. *11*, 845–850.

51. Virmani, M.A., and Cirulli, M. (2022). The role of l-carnitine in mitochondria, prevention of metabolic inflexibility and disease initiation. Int. J. Mol. Sci. *23*, 2717.

52. Jeon, S.M. (2016). Regulation and function of AMPK in physiology and diseases. Exp. Mol. Med. *48*, e245.

53. Huang, T.Y., Zheng, D., Houmard, J.A., Brault, J.J., Hickner, R.C., and Cortright, R.N. (2017). Overexpression of PGC-1α increases peroxisomal activity and mitochondrial fatty acid oxidation in human primary myotubes. Am. J. Physiol. Endocrinol. Metab. *312*, E253–E263.

54. Shao, L.R., Wang, G., and Stafstrom, C.E. (2018). The glycolytic metabolite, fructose-1,6-bisphosphate, blocks epileptiform bursts by attenuating voltage-activated calcium currents in hippocampal slices. Front. Cell. Neurosci. *12*, 168.

55. Lian, X.Y., Khan, F.A., and Stringer, J.L. (2007). Fructose-1,6-bisphosphate has anticonvulsant activity in models of acute seizures in adult rats. J. Neurosci. *27*, 12007–12011.

56. Cherkas, A., Holota, S., Mdzinarashvili, T., Gabbianelli, R., and Zarkovic, N. (2020). Glucose as a major antioxidant: when, what for and why it fails? Antioxidants *9*, 140.

57. Napoli, E., Wong, S., and Giulivi, C. (2013). Evidence of reactive oxygen species-mediated damage to mitochondrial DNA in children with typical autism. Mol. Autism. *4*, 2.

58. Rose, S., Frye, R.E., Slattery, J., Wynne, R., Tippett, M., Melnyk, S., and James, S.J. (2014). Oxidative stress induces mitochondrial dysfunction in a subset of autistic lymphoblastoid cell lines. Transl. Psychiatry *4*, e377.

59. Eltokhi, A., Janmaat, I.E., Genedi, M., Haarman, B.C.M., and Sommer, I.E.C. (2020). Dysregulation of synaptic pruning as a possible link between intestinal microbiota dysbiosis and neuropsychiatric disorders. J. Neurosci. Res. *98*, 1335–1369.

60. Castro, K., Baronio, D., Perry, I.S., Riesgo, R.D.S., and Gottfried, C. (2017). The effect of ketogenic diet in an animal model of autism induced by prenatal exposure to valproic acid. Nutr. Neurosci. *20*, 343–350.

61. Oyarzábal, A., Musokhranova, U., Lf, B., and García-Cazorla, A. (2021). Energy metabolism in childhood neurodevelopmental disorders. EBioMedicine *69*, 103474.

62. Karagiannis, A., Gallopin, T., Lacroix, A., Plaisier, F., Piquet, J., Geoffroy, H., Hepp, R., Naudé, J., Le Gac, B., Egger, R., et al. (2021). Lactate is an energy substrate for rodent cortical neurons and enhances their firing activity. Elife *10*, e71424.

63. Skwarzynska, D., Sun, H., Williamson, J., Kasprzak, I., and Kapur, J. (2022). Glycolysis Regulates Neuronal Excitability via Lactate Receptor (HCA1R. Brain), p. awac419.

64. Hollnagel, J.O., Cesetti, T., Schneider, J., Vazetdinova, A., Valiullina-Rakhmatullina, F., Lewen, A., Rozov, A., and Kann, O. (2020). Lactate attenuates synaptic transmission and affects brain rhythms featuring high energy expenditure. iScience *23*, 101316.

65. Margineanu, M.B., Mahmood, H., Fiumelli, H., and Magistretti, P.J. (2018). L-lactate regulates the expression of synaptic plasticity and neuroprotection genes in cortical neurons: a transcriptome analysis. Front. Mol. Neurosci. *11*, 375.

66. Herrera-López, G., Griego, E., and Galván, E.J. (2020). Lactate induces synapse-specific potentiation on CA3 pyramidal cells of rat hippocampus. PLoS One *15*, e0242309.

67. Bauernfeind, A.L., Barks, S.K., Duka, T., Grossman, L.I., Hof, P.R., and Sherwood, C.C. (2014). Aerobic glycolysis in the primate brain: reconsidering the implications for growth and maintenance. Brain Struct. Funct. *219*, 1149–1167.

68. Goyal, M.S., Hawrylycz, M., Miller, J.A., Snyder, A.Z., and Raichle, M.E. (2014). Aerobic glycolysis in the human brain is associated with development and neotenous gene expression. Cell Metab. *19*, 49–57.

69. Shannon, B.J., Vaishnavi, S.N., Vlassenko, A.G., Shimony, J.S., Rutlin, J., and Raichle, M.E. (2016). Brain aerobic glycolysis and motor adaptation learning. Proc. Natl. Acad. Sci. USA *113*, E3782–E3791.

70. van Heerden, J.H., Bruggeman, F.J., and Teusink, B. (2015). Multi-tasking of biosynthetic and energetic functions of glycolysis explained by supply and demand logic. Bioessays *37*, 34–45.

STAR★METHODS

KEY RESOURCES TABLE

REAGENT or RESOURCE	SOURCE	IDENTIFIER
Antibodies		
Rabbit anti-GLUT1	Novus Biological	Cat# NB110-39113
Rabbit anti-MCT1	Alomone Labs	Cat# AMT-011; RRID: AB_2756669
Anti-Rabbit IgG HRP Conjugate antibody	Promega	Cat# W4011; RRID: AB_430833
Rat anti-CD31	BD pharmingen	Cat#553370; RRID: AB_394816
Rabbit anti-GLUT3	ProteinTech	Cat#20403-1-AP; RRID: AB_10694437
Rabbit anti-hexokinase-1	Abcam	Cat# ab150423; RRID: AB_2920536
Rabbit anti-hexokinase-2	Abcam	Cat# ab209847; RRID: AB_2904621
Rabbit anti-GSK3b	Cell Signaling	Cat#12456; RRID: AB_2636978
Rabbit anti-AMPK	Cell Signaling	Cat# 2532; RRID: AB_330331
Rabbit anti-phospho-AMPK	Cell Signaling	Cat# 2535; RRID: AB_331250
Mouse anti-DRP1	BD Biosciences	Cat#611113; RRID: AB_398424
Mouse anti-MFN1	Abcam	Cat# ab126575; RRID: AB_11141234
Mouse anti-MFN2	Abcam	Cat# ab56889; RRID: AB_2142629
Rabbit anti-OPA1	Abcam	Cat# ab42364; RRID: AB_944549
Mouse anti-tubulin	Sigma Aldrich	Cat# T6199; RRID: AB_477583
Mouse anti-PGC-1α	Millipore Sigma	Cat# ST1202; RRID: AB_2237237
Mouse anti-GAPDH	ProteinTech	Cat# 60004-1-Ig; RRID: AB_2107436
Rabbit anti-Vinculin	Abcam	Cat# ab129002; RRID: AB_11144129
Donkey anti-Rat IgG (H + L) Highly Cross-Adsorbed Secondary Antibody, Alexa Fluor 488	Invitrogen	Cat#A-21208; RRID: AB_2535794
Donkey anti-rabbit IgG (H + L) Highly Cross-Absorbed Secondary Antibody, Alexa Fluor 568	Invitrogen	Cat#A-10042; RRID: AB_2534017
Chemicals, peptides, and recombinant proteins		
Anhydrous dextrose (glucose injections)	EMD Millipore Sigma	Cat # DX0145
DL-Lactic acid (lactate injections)	Acros Organics	Cat # AC125060250
Dr-Fructose (fructose injections)	Fisher Scientific	Cat #L95-500
β-hydroxybutyrate (BHB injections)	Sigma Aldrich	
PhosSTOP EASYpack (phosphatase inhibitor cocktail tablets)	Millipore Sigma	Cat# 4906837001
HBSS without calcium/magnesium	Gibco	Cat #14170-120
Fish gelatin blocking agent (10X)	Biotium	Cat#22010
Donkey serum, sterile filtered	Wisent Bioproducts	Cat#035-150
Fluoromount-G™	Electron Microscopy Sciences	Cat#17984-25
Paraformaldehyde 20% Solution, EM grade	Electron Microscopy Sciences	Cat#15713-S
Attachment factor 1X	Gibco	Cat#S-006-100
Albumin, Bovine (BSA)	VWR	Cat#0332-100G
CD31 microbeads, Mouse	Miltenyi Biotec	Cat#130-097-418
EGM™-2 MV Microvascular Endothelial Cell Growth Medium-2 BulletKit™	Lonza	Cat#CC-3202
GX Stain-free FastCast 12% Biorad gels	Bio-Rad	Cat#1610184
SuperSignal™ West Pico PLUS Chemiluminescent Substrate	Thermo Scientific	Cat# 34579
Rose Bengal	Alfa Aesar	Cat# A17053
Evans Blue	Sigma Aldrich	Cat# E2129-10G
Potassium Ferrocyanide	BioShop	Cat#PFC232.250

(*Continued on next page*)

Continued

REAGENT or RESOURCE	SOURCE	IDENTIFIER
Osmium Tetroxide 4% Aqueous Solution	Electron Microscopy Sciences	Cat# 19150
Thiocarbohydrazide	Electron Microscopy Sciences	Cat#21900
Trichloroacetic acid	Sigma Aldrich	Cat#T0699
Durcupan ACM Epoxy Resin Component B	Electron Microscopy Sciences	Cat#14042B
Critical commercial assays		
Pierce™ BCA Protein Assay Kit	Thermo Scientific	Cat #23227
Neural Tissue Dissociation Kit (P)	Miltenyi Biotec	Cat#130-092-628
Experimental models: Organisms/strains		
Mouse: B6129S-Del(7Slx1b-Sept1)4Aam/J (*16p11.2*$^{df/+}$)	Jackson Laboratory	Stock #013128; RRID: IMSR_JAX:013128
Mouse: B6129SF1/J	Jackson Laboratory	Stock #101043; RRID: IMSR_JAX:101043
Mouse: B6N.129P2(Cg)-Igs13tm1Dolm Igs14tm1Dolm/J (*16p11.2*$^{flox/+}$)	Jackson Laboratory	Stock #025330; RRID: IMSR_JAX:025330
Mouse: B6.FVB-Tg(Cdh5-cre)7Mlia/J (*Cdh5-Cre*$^{tg/+}$)	Jackson Laboratory	Stock #006137; RRID: IMSR_JAX:006137
Oligonucleotides		
Primer:*16p11.2*$^{df/+}$ Forward:5′-CCTCATGGACTAATTATGGAC-3′	This paper	N/A
Primer:*16p11.2*$^{df/+}$ Reverse: 5′-CCAGTTTCACTAATGACACA-3′	This paper	N/A
Primer: *16p11.2*$^{flox/+}$ Forward (p26): 5′-TTCGGCTTCTGGCGTGTGAC-3′	This paper	N/A
Primer: *16p11.2*$^{flox/+}$ Forward (p301): 5′-TTGGACAGACCCTGGTTCAGTC-3′	This paper	N/A
Primer: *16p11.2*$^{flox/+}$ Reverse (p132): 5′-GGTGGATGTGGAATGTGTGCGAG-3′	This paper	N/A
Primer: *Cdh5-Cre* Forward: 5′-GCAAGTTGAATAACCGGAAATGGTT-3′	This paper	N/A
Primer: *Cdh5-Cre* Reverse: 5′-AGGGTGTTATAAGCAATCCCCAGAA-3′	This paper	N/A
Software and algorithms		
Fiji ImageJ	https://imagej.net/software/fiji/	N/A
Metaboanalyst 5.0	https://www.metaboanalyst.ca	N/A
GraphPad Prism 9	https://www.graphpad.com/scientific-software/prism/	N/A
Other		
Glucose sensing electrode	Pinnacle Technology, Inc.	Cat # 7004
Lactate sensing electrode	Pinnacle Technology, Inc.	Cat # 7004
Cannulas	Pinnacle Technology, Inc.	Cat #7032
Vevo LAZR-X high frequency ultrasound and Photoacoustic Imaging (PAI)	FUJIFILM VisualSonics	N/A
LS columns	Miltenyi Biotec	Cat#130-042-401
MACS® MultiStand	Miltenyi Biotec	Cat#130-042-303
QuadroMACS™ separator	Miltenyi Biotec	Cat#130-090-976
FEI Tecnai Spirit G2 transmission electron microscope with a Hamamatsu ORCA-HR digital camera	FEI Company	N/A
Zeiss Axio Imager M2 microscope	Zeiss	N/A
ApoTome.2 module	Zeiss	N/A

RESOURCE AVAILABILITY

Lead contact

Further information and requests for resources should be directed to the lead contact, Dr. Baptiste Lacoste (blacoste@uottawa.ca).

Materials availability

This study did not generate new unique reagents.

Data and code availability

- All data reported in this paper will be shared by the lead contact upon request.
- This paper does not report original code.
- Any additional information required to reanalyze the data reported in this paper is available from the lead contact upon request.

EXPERIMENTAL MODEL AND SUBJECT DETAILS

All animal procedures were approved by the University of Ottawa Animal Care Committee and were conducted in accordance with the Canadian Council on Animal Care guidelines.

Mouse husbandry

All experimental mice used in this study were male mice. All mice were bred in house and housed maximum five per cage with free access to water and food. Mice subjected to awake monitoring of brain metabolites were kept on a reverse light cycle. Males *16p11.2*$^{df/+}$ (Jackson laboratory, stock #013128; mixed B6/129 background) were crossed with WT females of the same background (Jackson laboratory, stock #101043) to obtain hemizygous *16p11.2*$^{df/+}$ offspring as well as WT littermates. As recommended by Jackson Laboratory to improve *16p11.2*$^{df/+}$ pup survival, breeding cages (both constitutive and conditional mutants) were supplemented with breeding chow (#2019, Envigo Teklad) and DietGel (#76A, ClearH$_2$O) up to weaning age.[6] Testing procedures were conducted with mice aged p > 50. Conditional *16p11.2*$^{\Delta EC}$ mutants (*Cdh5-Cre*$^{tg/+;}$*16p11.2*$^{flox/+;}$ mixed B6/129 background) and littermate controls were obtained from breeding between *Cdh5-Cre*$^{tg/+}$ males (Jackson laboratory, stock #006137) and *16p11.2*$^{flox/+}$ females (Jackson laboratory, stock #025330).

Genotyping

16p11.2$^{df/+}$ and control littermates (WT) mice were genotyped using the following primers: 5′-CCTCATGGACTAATTATGGAC-3′ (forward) and 5′-CCAGTTTCACTAATGACACA-3′ (reverse) with a PCR product of 2.2Kb for *16p11.2*$^{df/+}$ mice. Conditional *16p11.2*$^{\Delta EC}$ mutants (*Cdh5-Cre*$^{tg/+;}$*16p11.2*$^{flox/+}$) were genotyped as follows. For *Cdh5-Cre*$^{tg/+}$, the following primers were used: 5′-GCAAGTT GAATAACCGGAAATGGTT-3′ (forward) and 5′-AGGGTGTTATAAGCAATCCCCAGAA-3′ (reverse), with a 250bp PCR product. For *16p11.2*$^{flox/+}$ genotyping, the following three primers were used: 5′-TTCGGCTTCTGGCGTGTGAC-3′ (p26, forward), 5′-TTGGACA GACCCTGGTTCAGTC-3′ (p301, forward) and 5′-GGTGGATGTGGAATGTGTGCGAG-3′ (p132, reverse), with two PCR products of 431bp and 341bp in length.

METHOD DETAILS

FDG-PET scan

Mice were fasted for 8 h prior to imaging and anesthetized by isoflurane. A tail vein cannula was inserted prior to being placed in a custom 4-position multi-animal hotel secured to the gantry of an Inveon D-PET scanner (Siemens). Mice were kept warm during the duration of the PET scan, which was followed by a 10 min transmission scan acquired under standard conditions. Once aligned in the PET field of view, a 45-min acquisition protocol in list mode format was initiated and approximately 200 μCi [^{18}F]-2 fluoro-D-deoxyglucose (FDG) was injected *intravenously* exactly 30 s afterward. Iterative reconstruction was performed using 3D ordered-subsets expectation maximisation (3D-OSEM) followed by fast maximum *a posteriori* (fastMAP) with the following parameters: MAP OSEM iterations, 2; MAP subsets, 16; MAP iterations, 18. Under anesthesia, mice were immediately transferred to a 3.0 T pre-clinical MRI (MR Solutions Inc.), and a T_2-weighted, axially sectioned, respiratory-gated Fast Spin Echo image of the head was acquired with the following parameters: 31 slices; 0.5 thickness and 0.1 spacing; FOV = 30 with FOV ratio = 0.75; TR = 4800, TE = 68, nex = 4. VivoQuant was used for visualization of radiotracer uptake in the brain, to align PET with MRI images, and to segment the brain into individual brain regions using a proprietary mouse brain atlas algorithm (VivoQuant v. 4.0, InviCRO, LLC). The count densities were averaged for all volumes of interest at each time point to obtain a time *versus* activity curve for the entire brain, and average count densities were averaged for each brain region analyzed for a bin spanning 40 to 45 min post-FDG injection. All quantified data were normalized to injected dose, measured by a CRC-15 PET dose calibrator (Capintec Inc), and expressed as percentage injected dose per mL of tissue (%I.D./mL).

For *in situ* autoradiography, fasted mice were administered 500 μCi of FDG by *intravenous* bolus injection under isoflurane anesthesia, followed by euthanasia by exsanguination *via* cardiac puncture 45 min after radiotracer injection. Cardiac perfusion was performed with saline to clear blood from tissues, and brains were resected and frozen in optimal cutting temperature medium compound (Tissue-Tek) on dry ice. Frozen blocks were equilibrated to −20°C for 30 min prior to sectioning. Tissue 12 μm-thick sections

were mounted onto microscope slides, air dried for 5 min, and exposed to a [^{18}F]-sensitive storage phosphor screen (PerkinElmer) overnight at 4°C. Screens were scanned on a Cyclone Storage Phosphor System (PerkinElmer), and image data was processed with ImageJ.

Extracellular brain glucose and lactate measurements

Surgery

Pre-surgical treatment included a 0.6 mg/kg subcutaneous (s.c.) injection of slow-release buprenorphine (Chiron Compounding Pharmacy Inc, Guelph, ON, CAN) and 1 mL of 0.9% saline (Hospira, QC, CAN). Immediately prior to surgery, mice were anesthetized using 4–5% isoflurane (Fresenius Kabi Canada Ltd., ON, CAN) then secured to a stereotaxic frame (David Kopf Instruments, Tujunga, CA, USA). Mice were maintained under anesthesia during the surgery with 1–2.5% isoflurane and kept warm with a heated pad (TP650, Gaymar Industries, Orchard Park, NY, USA). Based on the stereotaxic atlas of Franklin and Paxinos, two guide cannulas (BASi cannula Bioanalytical Systems, West Lafayette, IN) were positioned above the left and right primary motor cortex. The target coordinates, from bregma, were ±1.8 mm lateral and +1.0 mm anterior. The cannulas were positioned just beneath the skull surface so that the sensing cavity (1 mm) of the electrochemical electrode would protrude, when inserted at the time of testing. These guide cannulas were fixed using a UV-polymerized compound (UV Clear Fly Finish, Ashland, OR, USA) applied around four 0.10″-inch skull screws positioned anterior and posterior to the two guide cannulas. Post-surgical analgesia included application of 0.1 mL of transdermal bupivacaine (Chiron Compounding Pharmacy Inc., ON, CAN) around the incision area. After surgery, the mice were individually housed for 7 days to allow recovery and limit possible incidents with the newly inserted cannulas.

Electrodes

Briefly, extracellular brain levels of glucose and lactate were measured using two platinum enzyme-linked electrodes (7004-Glucose-C and 7004-Lactate-C; Pinnacle Technology Inc., Lawrence, KS, USA). Sensors were prepared from Pt-Ir wire of 180 μm diameter, wrapped concentrically with an AgCl reference electrode. Near the tip of the electrode, a 1 mm section is coated with either glucose or lactate oxidase. These enzymes oxidize the analytes of interest, resulting in an equivalent release of hydrogen peroxide (H_2O_2). H_2O_2 is subsequently detected and recorded as an amperometric oxidation current at the electrode. Data was collected at 1 Hz, transmitted from a potentiostat to a computer and recorded using the Sirenia Acquisition Software (Pinnacle Technology Inc., Lawrence, KS, USA). In addition to the oxidase enzymes, the metabolite sensitive surface is also coated with a series of membranes to increase the specificity and selectivity of the electrodes. For example, the potential contribution of ascorbic acid is reduced with the presence of ascorbic acid oxidase. These particular enzymes convert the electroactive ascorbate, which has the potential to interfere with the electrode's recordings, to non-electroactive dehydroascorbate and water.

Calibration

Immediately prior to and following *in vivo* testing, the electrodes were calibrated according to factory recommendations. Briefly, the electrodes were gently placed in 100 mM PBS (pH 7.4) at 23°C (pre-testing) or 37°C (post-testing) and tested for metabolite sensitivity by adding glucose (1 mM) and lactate (0.1 mM) to the PBS solution, as well as selectivity with the use of a single ascorbic acid (0.25 mM) addition. Pre-calibration curves demonstrated high sensitivity with incremental linear increases for both glucose (average sensitivity 0.314 nA/1mM) and lactate (average sensitivity 0.023 nA/0.1 mM) electrodes. Both glucose and lactate electrodes also exhibited high levels of selectivity by demonstrating minimal sensitivity to ascorbic acid (average sensitivity 0.143 nA/0.25 mM and 0.206 nA/0.25 mM, respectively). The post-calibration curves suggested a certain level of wear on the electrodes, most likely due to the insertion and removal process of these sensitive testing instruments. Similar results were obtained with linear increases for both glucose (average sensitivity 0.447 nA/1mM) and lactate (average sensitivity 0.068 nA/0.1 mM) electrodes. Post calibration curves for ascorbic acid found increased sensitivity to ascorbic acid for the lactate electrodes (average sensitivity 0.038 nA/0.25 mM and 2.159 nA/0.25 mM for glucose and lactate, respectively).

Testing Procedure

Seven days following surgery, and immediately after electrode calibration, the mice were briefly anesthetized with 1.5–2% isoflurane and the electrodes were inserted into the motor cortex through the surgically implanted guide cannulas and attached to the pre-amplifier. Mice were tested for two days in a custom-made square polymethyl methacrylate-testing cage with standard bedding (Teklad 7097 Corncob bedding, Envigo, ON, CAN) and water. A mounted camera (Pinnacle Technologies) above the cage recorded the duration of the testing and was synchronized with the electrode sampling. Mice had free access to water, but chow was removed 2 h prior to injection to ensure similar fasting states between the mice and returned after the last manipulation. Given that previous work demonstrated that extracellular brain concentrations of glucose and lactate stabilize within 2 h post-injection and that the intracortical electrodes reliably measured extracellular concentrations for at least 48 h, mice received 2 injections a day (10am and 1pm) for 2 days. The mice received a 2 g/kg intraperitoneal (i.p.) injection of either of either glucose (Dextrose Anhydrous, EMD Chemicals, Gibbstown, NJ, USA), lactate (Lactic Acid, Acros Organics, NJ, USA), fructose (D-Fructose, Fisher Scientific, Fair Lawn, NJ, USA) or β-hydroxybutyrate, BHB (Sigma Aldrich, St. Louis, MO, USA) in a counterbalanced order.

Two hours after each injection, the mice were placed on a vertical metal mesh (10 × 17 inches) with half-inch square holes. The mesh was held vertically while the mouse was left free to explore for 2 min. This approach was chosen following internal testing. Other tasks proved either proved too challenging with sensitive testing equipment (e.g., rotarod or treadmill) or unreliable in terms of measurements or mouse behavior. For example, using a running wheel within the caged resulted in irregular running bouts that were not consistent in intensity or duration, making comparisons challenging. In addition, during our trials we observed the well-documented

phenomenon of metabolic efficiency that comes with practice. To avoid missing metabolite fluctuations as a result of habituation, we opted for an ecological that it did not require training but result in robust metabolite fluctuations. These preliminary efforts indicated that the grid climb was a behavior the mice readily engaged in with no prior training while resulting in regular and robust fluctuations of extracellular brain glucose and lactate that were similar to the documented pattern expected to occur following neuronal activation.

Photoacoustic imaging

Imaging was performed using the Vevo LAZR-X high-frequency ultrasound and photoacoustic imaging (PAI) system (FUJIFILM VisualSonics, Toronto, Canada). All images were acquired using the MX250 21MHz linear array transducer, fitted with medium sized optical fibers. Animals were anesthetized with a xylazine/ketamine cocktail (0.1 mL/100 g). The head of each animal was secured and stabilized using a stereotactic frame attached to the imaging platform. Key physiological parameter such as heart rate, respiration rate and temperature were monitored throughout the imaging session. B-mode imaging was used for region of interest selection, followed by PAI mode. 2-D and 3-D PAI images were acquired under Oxy-Hemo Mode, using dual-wavelength imaging, alternating between 750nm and 850nm, for real-time display of oxygen saturation (sO_2). All 3D data were acquired by moving the transducer with a stepper motor, at a step size of 254μm.

Peripheral measurements of glucose metabolism

Body composition analysis

Total fat and lean mass were assessed using a nuclear echo magnetic resonance imaging (MRI) whole-body composition analyzer.

Glucose tolerance test

Experimental mice were food-deprived during 4 h with *ad libitum* access to water. A bolus of glucose (1.5 g/kg of body weight or lean body weight) was administered via an intraperitoneal (i.p.) injection and glycemia was measured from blood sampled at the tail vein using a Accu-chek Performa glucometer at T0 (before injection), 15, 30, 45, 60, 90 and 120 min. Tail vein blood samples were collected via a capillary for insulin assays at T0, 15 and 30 min.

Insulin tolerance

Experimental mice were food-deprived during 4 h with *ad libitum* access to water. A bolus of insulin (0.2U/kg of body weight) was administered via an intraperitoneal (i.p.) injection and glycemia was measured from blood sampled at the tail vein using a Accu-chek Performa glucometer at T0 (before injection), 15, 30, 45, 60, 90 and 120 min.

Western blot on cerebral cortex or brain endothelial cell lysates

Tissue preparation

All mice were euthanized by cervical dislocation. For cerebral cortex proteins, the brains rapidly removed in cold 1M PBS and the cerebral cortex was then microdissected and kept on ice. The cortex was then mechanically dissociated in RIPA buffer (NaCl 150mM, Sodium Deoxycholate 12mM, SDS 3.5mM, Tris 50mM, Triton X-100 1%v/v, pH 8.0) with protease and phosphatase inhibitors. The cell suspension was homogenized via ice-cold sonication, mixed at 4°C for 15 min then centrifuged (13,000rpm for 20 min at 4°C). The protein concentration of supernatant was quantified using Pierce BCA Protein assay (kit #23227, Thermo Scientific, Illinois, USA). For endothelial proteins, the cerebral cortex was dissected in cold HBSS without calcium and magnesium using autoclaved tools submerged in 100% ethanol for 30 min prior dissections. The cortex was minced in 2–3 mm pieces and dissociated in Neural Tissue Dissociation Kit P compounds (Miltenyi Biotec, 130-092-628) to obtain a cell suspension. Cell isolation procedures were completed according to the manufacturer's instructions. The cell suspension was incubated with CD31-coated magnetic microbeads (Miltenyi Biotec, 130-097-418) and placed on a magnetic MACs separator to isolate endothelial cells (ECs). ECs isolated from one mouse were seeded in 2 wells of a 6-well plate coated with attachment factor protein 1X (ThermoFisher Scientific, S006100). For a pure EC population, ECs were cultured in an EC specific medium (Lonza, CC-3202) which was replaced 48 h post-seeding and every 48 h until 100% confluency was reached for subsequent protein extraction. To lyse cells, 50uL of RIPA buffer (NaCl 150mM, Sodium Deoxycholate 12mM, SDS 3.5mM, Tris 50mM, Triton X-100 1%v/v, pH 8.0) with protease and phosphatase inhibitors was added to each well and left on ice for 30 min. The supernatant was transferred to a 1.5mL tube and then centrifuged at 13,000rpm for 10 min. The protein concentration of the collected supernatant was quantified using Pierce BCA Protein assay (kit #23227, ThermoScientific, Illinois, USA).

Immunoblotting

Fifteen (15) μg of protein were loaded into the wells of SDS-acrylamide gels (GX Stain-free FastCast 12% Biorad gels, Bio-Rad, ON, CAN, #1610184) and separated by a constant current of 100 V for 120 min in running buffer (SDS 35mM, Tris 250mM, Glycine 1865mM). After UV activation of the gels, the proteins were then transferred to a nitrocellulose membrane in ice-cold transfer buffer (Tris 48mM, Glycine 38mM, methanol 20% v/v) for 30 min at 100 V. After the transfer, the nitrocellulose membranes and gels were imaged to quantify the total protein transferred. The membranes were then blocked with 5% skim milk in 1M PBS for 1 h at room temperature and incubated with primary antibodies raised again either MCT-1 (1:200, Alomone, #AMT-011), GLUT-1 (1:1000, Novus-Bio, #NB110-39113), GLUT-3 (1:2000, ProteinTech, 20403-1-AP), hexokinase-1 (1:1500, Abcam, ab150423), hexokinase-2 (1:1500, Abcam, ab209847), GSK3β (1:3000, Cell Signaling, 12456), AMPK (1:1000, Cell Signaling, 2532), phospho-AMPK (1:800, Cell Signaling, 2535), DRP1 (1:2000, BD Biosciences, 611113), MFN1 (Abcam, ab126575, 1:1000), MFN2 (1:1000, Abcam, ab56889), OPA1 (1:2000, Abcam, ab42364), tubulin (1:5000, Sigma, T6199), PGC-1α (1:1500, Millipore, ST1202), GAPDH

(1:10000, ProteinTech, 60004-1-Ig) or Vinculin (1:5000, Abcam, ab129002) in TBST (Tris 50mM, NaCl 150mM, Tween 20 1% v/v) overnight at 4°C. The membranes were then washed with TBST (3 × 10 min) and incubated at room temperature for 1 h with the secondary antibody (1/10,000, Fisher Scientific, #PR-W4011), also diluted in TBST. After a final wash (TBST, 3 × 10 min), the proteins were detected by enhanced chemiluminescence (ECL; ¼, Fisher Scientific, #34579) and imaged with the Odyssey Imaging system. The samples were normalized to the total protein content (GLUT1, GLUT3, MCT1, hexokinase-1&2, GSK3β and AMPK) or to a loading control (OPA1, DRP1, MFN1&2, PGC1α) and calculated as relative to group average.

Immunofluorescence

All mice were euthanized by cervical dislocation. Whole brains were fixedin 4% paraformaldehyde (PFA) overnight at 4°C. All brains were washed in PBS, submerged in 15% sucrose overnight, followed by 30% sucrose overnight, then embedded in OCT medium. Brains were cut coronally into 25-μm-thick serial sections using a cryostat (HM525 NX, ThermoScientific), and finally mounted on charged glass slides. Sections were blocked using a solution containing 10% donkey serum, 0.5% Triton X-100 in PBS (0.5% PBT) and 0.5% cold water fish skin gelatin, and incubated overnight at 4°C with primary antibodies anti-CD31 (1/200, BD Pharmingen, Cat# 553370), and anti-GLUT1 (1/200, Novus-Bio, Cat# NB110-39113). The following day, sections were washed with 0.5% PBT and incubated with species-specific AlexaFluor secondary antibodies (donkey anti-rat IgG (H + L) Highly Cross-Absorbed Secondary Antibody, Alexa Fluor 488, 1/300, Invitrogen, Cat# A-21208 and donkey anti-rabbit IgG (H + L) Highly Cross-Absorbed Secondary Antibody, Alexa Fluor 568, 1/300, Invitrogen, Cat# A-10042) for 2 h at room temperature. Sections were washed with 0.5% PBT and PB then coverslipped in Fluoromount G (EMS). Immunostained sections were examined using a Zeiss Axio Imager M2 microscope equipped with a digital camera (Axiocam 506 mono) and the Zeiss ApoTome.2 module for optical sectioning. Nine 20-μm-deep z-stacks were acquired at 20X per mouse (three images per brain section, three sections per brain). GLUT1 distribution was determined using Fiji-Image J. Images were converted to 8-bit, running the Z-Project with the Max Intensity setting to obtain a 2D image. The image threshold was determined using the Huang pre-set to acquire a binary image. Analyze Particles, with size set to 5-infinity, was used to find the proportion of the image containing the signal of interest. GLUT1 distribution on cortical vessels was quantified by analyzing the surface ratio of the total CD31-positive vessel surface area also positive for GLUT1.

Systemic glucose injections and tissue collection for metabolomics

Prior injections, mice had free access to water while chow was removed for 2 h to ensure similar fasted state. Groups of five (5) mice received an intraperitoneal (i.p.) injection of either 1x sterile 50mM PBS pH 7.4 (baseline group) or 2 g/kg of glucose (Dextrose Anhydrous, EMD Chemicals, Gibbstown, NJ, USA) for a final 1% body weight injection volume. All mice were euthanized by cervical dislocation at 5 min (PBS, glucose) or 15 min (glucose) following i.p. injection. The brain was extracted from the skull from which the cerebellum and brain stem were removed. The cerebral hemispheres were bisected along the midline for removal of the striatum, hippocampus and thalamus. After which, the intact cortex was further dissected to isolate ∼20mg of tissue per sample. The cortex was then flash-frozen and stored at −80°C before further processing for metabolite extraction (performed simultaneously for all mice).

Targeted metabolomics

Sample temperature was maintained on ice or dry ice where possible, and all solvents were MS grade and pre-equilibrated to −20°C. On the day of extraction, frozen brain tissue samples were grounded into powder using a mortar and pestle on liquid nitrogen. 20 mg tissues weighed in to a cold 2mL bead beater tube containing 4 ceramic beads (2.8 mm) and 50% methanol. Bead beating was done to homogenize the tissue sample with the addition of acetonitrile. Samples were then incubated with a 2:1 dichloromethane:water solution on ice for 10 min. The polar and non-polar phases were separated by centrifugation at 4000g for 10 min at 1°C. The upper polar phase was dried using a refrigerated CentriVap Vacuum Concentrator at −4°C (LabConco Corporation, Kansas City, MO). Samples were resuspended in water and run on an Agilent 6470A tandem quadruple mass spectrometer equipped with a 1290 Infinity II ultra-high performance LC (Agilent Technologies) utilizing the Metabolomics Dynamic MRM Database and Method (Agilent), which uses an ion-pairing reverse phase chromatography (https://www.agilent.com/cs/library/applications/5991-8073EN.pdf). This method was further optimized for phosphate-containing metabolites with the addition of 5 μM InfinityLab deactivator (Agilent) to mobile phases A and B, which requires decreasing the backflush acetonitrile to 90%. Multiple reaction monitoring (MRM) transitions were optimized using authentic standards and quality control samples. Metabolites were quantified by integrating the area under the curve of each compound using external standard calibration curves with Mass Hunter Quant (Agilent). No corrections for ion suppression or enhancement were performed, as such, uncorrected metabolite concentrations are presented. Statistical analysis was performed by one-way analysis of variance (ANOVA) followed by Tukey's post hoc test. p values < .05 were considered statistically significant. Data for group comparisons are presented as box and whisker plots and statistical analysis was performed by an unpaired t test. The box represents the 25–75 interquartile range, and the horizontal line represents the median value. The boxplot analysis was performed using Prism 7 (GraphPad Software, La Jolla, CA, USA). Multivariate statistical modeling was performed on log-transformed, mean-centered and pareto-scaled data using MetaboAnalyst 5.0 (www.metaboanalyst.ca). Before multivariate analysis, missing values were replaced with 1/3 of the limit of detection of each metabolite. Principal component analysis (PCA) and partial least squares discriminant analysis (PLS-DA) were performed on the identified metabolites. The variables highly contributing to the group separation were selected with a variable importance in projection (VIP) ≥ 1. The clustering analysis and pathway analysis were performed as well using MetaboAnalyst 5.0.

Transmission electron microscopy (TEM)

Mice were anesthetized with a ketamine/xylazine cocktail (1 mg/kg, intraperitoneally) and perfused through the aortic arch with 3.5% acrolein and 4% paraformaldehyde. Fifty-micrometer-thick coronal sections of the brains were cut in sodium phosphate buffer (PBS 50 mM, pH7.4) using a Leica VT1000S vibratome (Leica Biosystems) and stored at −20°C in cryoprotectant until further processing. Sections were post-fixed and embedded using variations of the protocol by Deerinck et al. (https://ncmir.ucsd.edu/sbem-protocol). In brief, the sections were washed 3 times in PBS for 10 min and incubated in 1.5% potassium ferrocyanide and 2% aqueous osmium tetroxide in 0.1M phosphate buffer (pH 7.4) for 1 h at room temperature. The sections were subsequently washed 5 times with double-distilled water (ddH_2O) for 3 min, then incubated 20 min in a fresh solution of thiocarbohydrazide (1% w/v) at room temperature. Sections were washed again 5 times with ddH_2O for 3 min, incubated 30 min in 2% aqueous osmium tetroxide, and washed 5 times with ddH_2O for 3 min. Sections were dehydrated using increasing ethanol concentrations followed by propylene oxide, and then embedded in Durcupan resin (Sigma-Aldrich) between ACLAR sheets at 55°C for 3 days. Ultrathin sections were generated at ~65 nm using a Leica UC7 ultramicrotome. Imaging was performed in the antero-frontal (2.8–1.98mm bregma) and parieto-somatosensory (−0.70 to −1.82mm bregma) areas. In each region, 10 capillaries were randomly photographed per mouse, ranging in diameter between 3 and 6 μm, using a FEI Tecnai Spirit G2 transmission electron microscope operating at 80kV and equipped with a Hamamatsu ORCA-HR digital camera (10 MP). For each capillary, an image at 4,800X was acquired, in addition to 1–3 images at 13,000X to generate a high-resolution mosaic of the capillary. Metrics included i) number of mitochondria normalized to cytoplasm area ($1/\mu m^2$); ii) total mitochondrial area normalized to cytoplasm area (%); iii) average size (nm^2) of individual mitochondria; iv) average maximal length (nm) of individual mitochondria; as well as v) aspect ratio of individual mitochondria (ratio between the major and minor axes of a mitochondrion); and vi) proportion of mitochondria display one or more cristae. All metrics were quantified manually from micrographs, using Polygon and Freehand Selection tools (mitochondrial and cytoplasmic area) or Straight Line (mitochondrial width, length), followed by the Measure function.

Photothrombotic (PT) stroke and Evans blue dye (EBD) leakage assay

To compared BBB integrity between WT and *16p11.2*$^{df/+}$ mice, we quantified of the parenchymal extravasation of EBD (70kDa) in cortical tissue lysates following retroorbital injection of the dye. In brief, mice were anesthetized with an i.p. injection of ketamine/xylazine cocktail (1 mg/kg). 2% Evans Blue Dye (EBD) solution was injected (3 mL/kg, 60 mg/kg) retro-orbitally. Body temperature was maintained during surgery at 37 ± 0.5°C using a heating pad. 1 h after EBD circulation, the mice were transcardially perfused with cold PBS. The cerebral cortex was isolated, weighed and homogenized in a sevenfold volume of 50% trichloroacetic acid (Sigma-Aldrich, T0699). After centrifugation (10,300 rpm for 20 min at 4°C), the supernatants were collected and then diluted fourfold with 100% anhydrous ethanol. Diluted samples were loaded into a 96-well plate. Fluorescence intensity was measured using a microplate fluorescence reader (620 nm excitation, 680 nm emission; Synergy H1 Hybrid Reader, BioTek). The extravasated dye was quantified using a standard curve and expressed as $ng.\mu g^{-1}$/mg of tissue. As a positive control to assess significant EBD leakage, we performed cortical focal PT stroke in WT mice. In brief, mice received an i.p. injection of light-sensitive dye Rose Bengal (RB, 100 mg/kg) while placed in a stereotaxic frame. RB will be allowed to circulate for 5 min, and a laser (530nm, 20mW) was placed 3 cm above the skull at coordinates used for targeting the M1 cortex. The laser remained ON for 10 min, activating RB and causing platelet aggregation and blood clot formation. The EBD leakage assay was performed as described above 24 h after stroke on cortical tissue extracts comprising the stroke core and peri-infarct region.

QUANTIFICATION AND STATISTICAL ANALYSIS

No statistical methods were used to pre-determine sample sizes, but our sample sizes are similar to those reported in previous publications (Ouellette et al., 2020). All animal numbers in this study are in line with well-accepted standards from the literature for each method. All data presented in this work were obtained from experimental replicates (i.e., multiple animal cohorts from different litters). All attempts of replication were successful. All data analysis was conducted blind to genotype/experimental condition. Groups were reassembled upon completion of data analysis according to genotype, age, sex. Randomization of individual samples/animals was performed by numbering. All statistical tests were performed using GraphPad Prism 9.0 Software. Data distribution was assumed to be normal, but this was not formally tested. Unpaired Mann-Whitney U test or t test (each animal being considered as a sample) was used for two-group comparisons between *16p11.2*$^{df/+}$ mice and control littermates for metrics such as average FDG uptake, oxygen saturation, total hemoglobin content, quantification of GLUT-1 and MCT-1, metabolite abundance, etc. A two-way ANOVA (e.g. 'genotype x time') and Sidak's *or* Tukey's *post-hoc* test was used for kinetics of FDG uptake, oxygen saturation, extracellular brain metabolite fluctuations, etc. $p < 0.05$ was considered significant. Statistical details of each experiment can be found in figure legends.